Aerosols, Ice Supersaturation, and Cirrus Clouds in the Southern Hemisphere

Comparison of Aircraft Observations with Two Global Climate Models

Adam Sokol

Advisor: Trude Storelvmo

Second Reader: Ron Smith

May 5, 2017

A Senior Thesis presented to the faculty of the Department of Geology and Geophysics, Yale University, in partial fulfillment of the Bachelor's Degree.

Abstract

Cirrus clouds play an important role in Earth's climate and remain one of the largest uncertainties in global climate models (GCMs). Aircraft observations of cirrus clouds and ambient environmental conditions in the upper troposphere provide a unique opportunity to evaluate and constrain the cirrus cloud parameterizations used in GCMs. In this study, observations from three recent aircraft campaigns are used to characterize relative humidity with respect to ice (RHi), cirrus cloud microphysics, and aerosol concentrations in the Southern Hemisphere and to evaluate the performance of two GCMs: the Community Atmosphere Model 5 and ECHAM6 coupled with the Hamburg Aerosol Module HAM2. Analysis of the RHi observations reveals that ice nuclei are occasionally absent in the upper troposphere, allowing homogeneous ice nucleation to occur. However, observations of cirrus cloud ice crystal number concentration (N_i) indicate that heterogeneous ice nucleation contributes substantially to cloud formation. ECHAM-HAM largely overestimates both in-cloud and clear-sky RHi, while CAM5 is relatively accurate. The accuracy of N_i simulated by ECHAM-HAM varies over the altitude range considered, whereas CAM5 overestimates N_i by one to two orders of magnitude at all altitudes. Biases in model predictions of N_i are likely due to unrealistic treatment of detrained ice crystals, but may also be influenced by the competition between homogeneous and heterogeneous nucleation. Both models underestimate the concentration of accumulation mode aerosols and fail to capture the observed spatial variation in condensation nuclei concentration. These results highlight the importance of heterogeneous nucleation in the Southern Hemisphere and underscore the need for further improvement of model parameterizations governing cirrus clouds.

---

1 Introduction

Cirrus clouds are ice clouds in the upper troposphere that cover about 30% of Earth's surface (Stubenrauch et al., 2006) and remain one of the largest sources of uncertainty in climate models (Dufresne and Bony, 2008; Soden and Held, 2006; Zelinka et al., 2012; Zelinka et al., 2013). Cirrus contribute to Earth's albedo by reflecting incoming solar radiation and enhance the

greenhouse effect by absorbing outgoing longwave radiation and emitting it to space with reduced intensity. These radiative effects are influenced by cloud microphysical properties, such as ice crystal size and number concentration (Mitchell et al., 2008), which are themselves largely modulated by the initial conditions of cloud formation in the upper troposphere, such as relative humidity with respect to ice (RHi) and aerosol availability. In order to understand the complex role of cirrus clouds in Earth's climate system, it is necessary to understand both the initial conditions of cirrus formation and the resulting microphysical properties.

Ice nucleation mechanism plays an important role in determining cloud microphysical properties and has important climatic impacts (Gettelman et al., 2012). Ice crystals (IC) form either by homogeneous or heterogeneous nucleation depending on ambient conditions. Homogeneous nucleation, the theory of which is well understood (Koop et al., 2000), involves the spontaneous nucleation of ice within a liquid solution droplet at temperatures below -35°C and high RHi (~ 150%) (Pruppacher and Klett, 1997). On the other hand, heterogeneous nucleation can drive IC formation at minimal vapor supersaturation (RHi > ~100%) beginning at 0°C (Hoose and Möhler, 2012). Heterogeneous nucleation requires the presence of an insoluble substrate called an ice nuclei (IN) and can itself occur by a variety of mechanisms, including direct contact (IN collides with liquid drop), immersion (IN previously immersed in drop), condensation (liquid condensation onto IN), and deposition (formation of ice germ directly from the vapor phase on IN surface). Mineral dust and metallic particles are the dominant sources of IN, through other materials such as anhydrous salts and biological materials are capable of acting as IN as well (Cziczo et al., 2013). Typically, homogeneous nucleation results in smaller IC and larger IC number concentration (N_i) than heterogeneous nucleation. It has been suggested that homogeneous nucleation is the dominant mechanism of cirrus cloud formation in the upper troposphere (Gallagher et al., 2005; Heymsfield and Miloshevich, 1995; Karcher and Lohmann, 2003), but several studies have shown that heterogeneous nucleation can also play an important role (Cziczo et al., 2013; Haag et al., 2003; Jensen et al., 2013).

The competition between homogeneous and heterogeneous nucleation has important implications for the viability of cirrus cloud seeding as a possible climate engineering mechanism. This idea, first put forth by Mitchell and Finnegan (2009), involves the artificial injection of efficient IN to drive heterogeneous nucleation and prevent the high RHi needed for homogeneous nucleation. This would increase IC size and decrease N_i, mitigating the

greenhouse warming effects of cirrus clouds. Modeling studies by Storelvmo et al. (2014) and Storelvmo and Herger (2014) have shown that optimal seeding can decrease global temperature by 1.4°C and is most effective in regions with scarce IN, particularly the Southern Hemisphere (SH). On the other hand, Penner et al. (2015) and Gasparini and Lohmann (2016), using different model setups, found that seeding cannot significantly cool climate. Because the goal of seeding is to decrease the occurrence of homogeneous nucleation, it will only be effective if homogeneous nucleation presently plays a significant role in cirrus formation. Since different model parameterizations predict different amounts of homogeneous and heterogeneous nucleation, it is necessary to improve and constrain model representations of cirrus formation in order to accurately evaluate the cooling potential of cirrus cloud seeding.

General circulation models (GCMs) are unable to resolve cloud-scale processes, and parameterizations still struggle to accurately simulate cirrus cloud formation, evolution, and microphysical properties (Eidhammer et al., 2014; Muhlbauer et al., 2015; Shi et al., 2015). Aircraft observations of RHi, aerosols, and cloud microphysical properties in the upper troposphere provide an opportunity to evaluate and constrain model parameterizations. Unfortunately, observations of upper tropospheric humidity and aerosol concentration are limited in their temporal and spatial coverage (Gettelman et al., 2006). Furthermore, the shattering of ice particles during contact with measurement probes has recently been recognized as a pervasive source of measurement error, calling into question the integrity of many past measurements of ice microphysics (Jensen et al., 2009; Korolev and Isaac, 2005; Korolev et al., 2011; McFarquhar et al., 2007). However, recent improvements in instrumentation and shattering correction methods have allowed for cirrus cloud measurement with enhanced accuracy.

Despite the limited availability of high-quality in situ observations, statistical comparison to model output can offer new perspective on model schemes. Several previous studies have evaluated GCM treatments of cirrus clouds by comparison to in situ observations (e.g., Eidhammer et al., 2014; Wu et al., 2017; Zhang et al., 2013). However, the majority of these studies have focused on the Northern Hemisphere (NH) due to a lack of aircraft measurements in the upper troposphere of the SH. Little is known about cirrus clouds in the mid- and high-latitudes of the SH and how they differ from those of the NH (Gasparini and Lohmann, 2016). It is generally thought that abundant anthropogenic emissions of IN in the NH drive heterogeneous nucleation, while the relative scarcity of IN in the SH allows homogeneous nucleation to

dominate (Haag et al., 2003). Recent studies have illuminated hemispheric differences in cirrus cloud properties and underscore the importance of a more global perspective on cloud microphysics and the initial conditions of cirrus formation. Gayet et al. (2004), Haag et al. (2003), and Strom et al. (2003) found hemispheric differences in aircraft measurements of several cirrus cloud properties. Ovarlez et al. (2002) and Gettelman et al. (2006) found that clear-sky ice supersaturation (ISS) frequency is higher in the SH than in the NH. On the other hand, Kahn et al. (2009) and Diao et al. (2014b) did not find a hemispheric difference in ISS frequency. A greater focus on the SH is needed to better understand hemispheric differences in cirrus clouds and to evaluate model performance without geographic bias.

The objective of this study is two-fold. Firstly, it seeks to characterize RHi, aerosol concentration, and cirrus cloud microphysics in of the southern mid-latitudes using in high-resolution, situ observations from three recent aircraft campaigns. Secondly, the performance of two general circulation models (GCMs) with respect to RHi, aerosol concentration, and cirrus microphysics will be evaluated in light of these observations. This study provides a much-needed focus on the SH and makes use of several observational datasets that have yet to be used for model evaluation or classification of cirrus cloud properties. Furthermore, whereas the geographic limitations of in situ observations have limited the spatial applicability of prior work, this study combines observations from different campaigns to provide a broader perspective of model performance

2 Methods

2.1 Observational Datasets and Instrumentation

The observations used in this study are 1 Hz in situ measurements made from the National Science Foundation Gulfstream V (NSF GV) research aircraft. Observations from three aircraft campaigns—DEEPWAVE, HIPPO, and ORCAS—are combined to provide a Southern Hemisphere dataset that spans various latitudes, longitudes, altitudes, and seasons. This study considers measurements from a total of 59 research flights (RFs) between 75°S and 9°S that provide a cumulative 381 hours of flight time. The flight tracks of the RFs considered are shown in Figure 1. Datasets were acquired from the data archive of the Earth Observing Laboratory

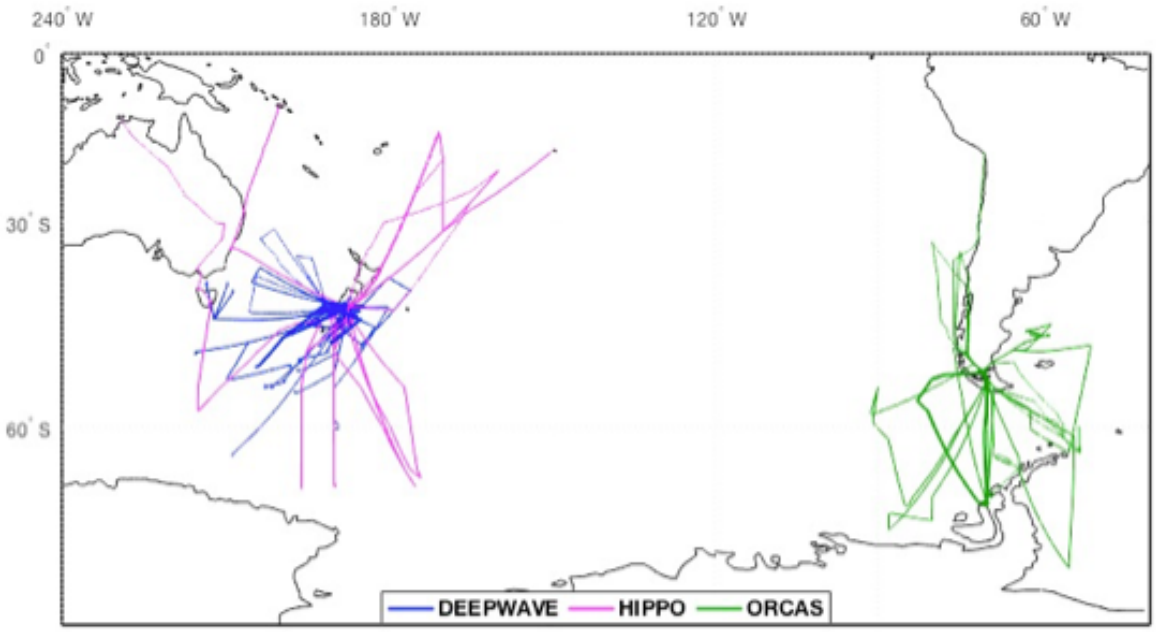

Figure 1. *Flight tracks of the research flights considered in this study. All altitudes are included. Thicker lines indicate multiple flights of the same path.*

(EOL) at the National Center for Atmospheric Research (https://data.eol.ucar.edu/). The accompanying documentation for each dataset was consulted as a guide to data quality.

The Deep Propagating Gravity Wave Experiment over New Zealand (DEEPWAVE) collected data primarily from the stratosphere over and around New Zealand in 2014 but offers a substantial amount of data from the upper troposphere as well (Fritts et al., 2016). Measurements from 26 DEEPWAVE research flights (RFs) were used in this study. The HIAPER Pole-to-Pole Observations (HIPPO) campaign provided vertical atmospheric transects over the Pacific Ocean over a wide range of latitudes (Wofsy et al., 2011). HIPPO was completed in five phases (hereafter referred to as HIPPO-1, HIPPO-2, etc.) between 2009 and 2011 and included flights in both the NH and SH. This study utilizes measurements from 15 HIPPO RFs—three in the SH from each of the five phases. The O_2/N_2 Ratio and CO_2 Airborne Southern Ocean Study (ORCAS) provided vertical transects over the Southern Ocean and parts of South America and Antarctica. Measurements from 18 ORCAS RFs were considered. Between the three aircraft campaigns, measurements from a total of 59 RFs providing over 381 hours of flight time were considered in this comparison. A summary of the aircraft campaigns the data that is available for each is presented in Table 1.

Table 1. Aircraft campaigns and data availability.

			HIPPO				
	DEEPWAVE	ORCAS	1	2	3	4	5
Date	Jun-Jul 14	Jan-Feb 16	Jan 09	Nov 09	Apr 09	Jun-Jul 11	Aug-Sep 11
Flights	26	18	3	3	3	3	3
Flight Time (Hrs.)	179	95	22	23	19	21	22
VCSEL	Yes	Yes	2/3 RFs	Yes	Yes	Yes	Yes
CN Counter	Yes	Yes	No	No	No	No	No
UHSAS	14 RFs	Yes	> 0.1μm	No	Yes	Yes	Yes
2DC Probe	No	Yes	No	Yes	Yes	Yes	Yes
CDP	No	Yes	Yes	Yes	Yes	Yes	Yes
ICNC (2DC + CDP)	No	Yes	No	Yes	Yes	Yes	Yes

Humidity and Temperature

Air temperature was measured by six different sensors aboard the GV aircraft: four heated sensors (Harco Model 100009-1), one high-rate sensor, and the aircraft avionics system. For each campaign, the investigators designated a "reference" air temperature measurement that is believed to be the most accurate and is suggested for use in thermodynamic calculations. The sensor that served as the source of the reference value varied between campaigns. The reference air temperature value was used to calculate the saturation vapor pressure of water with respect to ice following the method presented by Murphy and Koop (2005) (see Appendix, 8.1). RHi was then calculated from ambient water vapor pressure measurements from the 25-Hz vertical cavity surface-emitting laser (VCSEL) hygrometer mounted on the aircraft's fuselage (Zondlo et al., 2010). The open-path design of the VCSEL hygrometer allows for a fast response time and avoids the sampling effects associated with closed-path systems. The accuracy and precision of

the hygrometer are 6% and <3%, respectively. Water vapor measurements in the datasets had been averaged to 1 second for consistency with the frequencies of other measurements. Measurements from the VCSEL hygrometer were available across all three campaigns for all of the RFs except for RF08 of HIPPO-1, when the VCSEL hygrometer was inoperable.

Aerosol Particles

Condensation nuclei larger than 11 nm in diameter were measured during DEEPWAVE and ORCAS by a TSI-3760A butanol-based CN counter. Particles are exposed to supersaturated butanol vapor and the resulting droplets are detected by an optical counter. The CN counter can measure particles larger than the size threshold of 11 nm at concentrations up to 10,000 cm^{-3} with an accuracy of ±10% (http://www.tsi.com/condensation-particle-counter-3760a/).

Aerosol particles with a diameter between 0.06 μm and 1.0 μm were measured by an ultra-high sensitivity aerosol spectrometer (UHSAS; Droplet Measurement Technologies) during all campaigns with the exception of HIPPO-2. The UHSAS can measure particle concentrations up to 4,000 cm^{-3} in up to 100 size bins (http://www.dropletmeasurement.com/ultra-high-sensitivity-aerosol-spectrometer-uhsas). The datasets used in this study provided UHSAS concentration measurements for three size bins: 0.06-1.0 μm, 0.1-1.0 μm, and 0.5-1.0 μm. During HIPPO-1, particle counts were noisy and spurious for the smallest seven size bins measured by the UHSAS. As a result, the measurements for these bins were eliminated by EOL, setting the effective lower detection bound at 0.09 μm for HIPPO-1. Thus, this study incudes measurements for the 0.1-1.0 μm and 0.5-1.0 μm size bins from HIPPO-1 but does not include the UHSAS total count (0.06-1.0 μm).

Cloud Microphysics

Hydrometeor size and concentration measurements from two different instruments were included in this comparison. During ORCAS and HIPPO 2-5, hydrometeors were measured by a two-dimensional optical array cloud probe (Korolev et al., 2011). As hydrometeors pass through the probe's laser beam, their two-dimensional shadows are cast onto a linear diode array consisting of 64 photodiodes. The probe has a 25-μm resolution but does not return accurate concentration measurements particles in the smallest size bins. Following the recommendation of instrument experts, the effective lower size detection limit was taken to be 62 μm (Jensen, 2017).

The software used to process the 2DC measurements for the datasets considered in this study includes correction for particle shattering events following Field et al. (2006).

During HIPPO 1-5 and ORCAS, hydrometeors were also measured by a cloud droplet probe (CDP; Droplet Measurement Technologies). The CDP is a forward-scattering optical spectrometer capable of measuring 2-50 μm droplets at number concentrations up to 2,000 cm^{-3} (http://www.dropletmeasurement.com/cloud-droplet-probe-cdp-2). The particle size range of the instrument allows it to detected both liquid cloud droplets and small ice particles.

Neither the 2DC or the CDP alone can accurately measure total hydrometeor number concentration in ice or mixed-phase clouds due to their limited particle size ranges. Number concentration measurements from 2DC and CDP were added together to provide a better, albeit still incomplete, estimate of the number concentration of hydrometeors with diameters between 2 and 50 μm and greater than 62 μm (see Appendix, 8.1). At temperatures below -38°C—when liquid droplets cannot persist—hydrometeor number concentration measurements were taken to reflect N_i. Between -38°C and -35°C, both homogeneous and heterogeneous nucleation can occur (Pruppacher and Klett, 1997). In this temperature range, hydrometeor concentration measurements could include both liquid droplets and ice crystals. To distinguish between liquid droplets and ice crystals, measurements from a Rosemount Icing Detector (Model 871) were used to detect the presence of supercooled liquid water. The detector features an oscillating probe whose vibration frequency changes with ice accumulation. When the accumulated ice exceeds a threshold, the probe is heated briefly to remove the ice. The instrument's raw output (hereafter referred to as RICE), in Volts, was recorded during all RFs and increases in the presence of supercooled liquid water. It has been shown that the detector is quite sensitive to the presence of supercooled water and shows insignificant response in the presence of ice crystals (Cober et al., 2001). As a result, RICE can be used confidently to distinguish ice clouds from mixed-phase clouds in the -35°C to -38°C range.

Cloud Detection

Measurements were classified as in-cloud or clear-sky using several criteria. A summary of these criteria are presented in Table 2. HIPPO 2-5 and ORCAS provided both 2DC and CDP measurements, so a total N_i estimate could be derived. For $T < -38°C$, measurements were

Table 2. Criteria used for the cloudiness classification of ORCAS and HIPPO 2-5 measurements.

	In-Cloud (Cirrus)		Clear-Sky
Temperature	T < -38°C	-38°C < T < -35°C	T < -35°C
IC Number Conc.	$N_i > 1$ m^{-3}	$N_i > 1$ m^{-3}	$N_i < 1$ m^{-3}
Liquid Water Detection	N/A*	RICE < 1.6†	N/A‡
Number (Hours) of 1 Hz Measurements	7,031 (2.0)	935 (0.3)	118,096 (32.8)

*Liquid water cannot persist in this temperature range.
†See Figure 3.
‡While high RICE values do occur for a small number of clear-sky measurements, they are believed to be artifacts, as described in the text. As long as the clear-sky N_i criteria was met, measurements were classified as clear-sky regardless of their RICE value.

classified as in-cloud cirrus measurements if N_i exceeded 1 m^{-3}. For -38°C < T < -35°C, the same N_i threshold was used. However, in this temperature range, liquid cloud droplets can still be present. To distinguish ice clouds from mixed-phased clouds, a RICE threshold was selected by examination of HIPPO 2-5 and ORCAS clear-sky ($N_i < 1$ m^{-3}) RICE measurements, which represent the normal range of RICE in the absence of supercooled liquid water (Figure 2). It is visible in Figure 2 that the vast majority of clear-sky RICE measurements fall below 1.6 V. Thus, 1.6 V was selected as the threshold value. In-cloud measurements in the -38°C < T < -35°C range were thus considered to be cirrus measurements if RICE < 1.6 and mixed-phase measurements if RICE > 1.6.

The curved, upward deviations of RICE in Figure 3 indicate icing on the oscillating probe, suggesting that some of the measurements classified as clear-sky by N_i criteria were, in fact, taken in mixed-phase or liquid clouds. At warmer temperatures, high RICE values could be explained by the presence of liquid droplets smaller than 2 μm, which would go undetected by the CDP but would nonetheless cause a response in RICE. However, this does not explain the instance of high RICE values between -38°C and -61°C, since liquid water does not persist in the atmosphere at these temperatures. A closer examination of this flight (HIPPO-2 RF07) reveals that the aircraft was ascending through a cloud immediately prior to these measurements. RICE peaked at approximately -35°C and descended gradually for the next 20 minutes as the aircraft

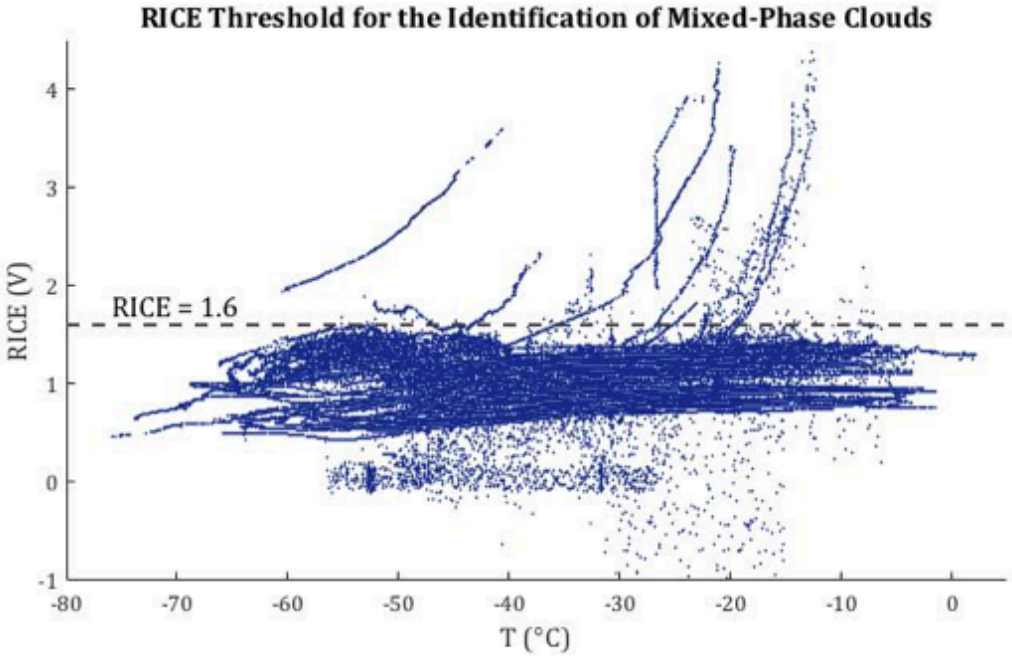

Figure 2. *Selection of the RICE threshold used to identify the presence of supercooled liquid water for HIPPO 2-5 and ORCAS. The continuous, curved lines indicate icing. The threshold of 1.6 was selected because it is the upper limit of RICE values recorded when there was no apparent icing.*

continued its ascent to much colder temperatures. It is possible that the peak icing at -35°C was not enough to trigger the sensor's heating mechanism. In that case, ice could have remained on the sensor for an extended period of time, slowly sublimating as the aircraft continued its ascent. The residual ice could explain the high RICE values in the absence of supercooled water. RICE would only return to its normal, clear-sky value once the residual ice had completely sublimated.

The cloud classification scheme outlined above and in Table 2 was not possible for DEEPWAVE and HIPPO-1 due to differences in instrumentation. There were no CDP or 2DC measurements taken during DEEPWAVE, so RICE is the only indicator of cloudiness. A RICE threshold of 1.47 was selected for DEEPWAVE, above which measurements were considered to be mixed-phase or liquid cloud measurements. However, since RICE does not detect the presence of IC, ice clouds in the -38°C < T < -35°C range and cirrus clouds in the T < -38°C range could not be identified. As a result, DEEPWAVE measurements were not included in any in-cloud or clear-sky analysis presented in Section 3.1 but are included in the analysis of overall RHi.

HIPPO-1 provided CDP but not 2DC measurements. Measurements were considered to be in-cloud if the CDP number concentration exceeded 1 m^{-3}. These measurements were

classified as cirrus measurements if T < -38°C or if -38°C < T < -35°C and RICE was less than the HIPPO-1 threshold of 1.0. These cirrus measurements were included in the analysis of in-cloud RHi in Section 3.1. However, since the CDP cannot detect IC larger than 50 μm, ICNC and IC size measurements for these clouds are inaccurate and were not considered in the analysis in Section 3.2. The remaining HIPPO-1 measurements, for which the CDP number concentration fell below 1 m^{-3}, could not be classified as clear-sky with high confidence, since the aircraft could have encountered ice clouds where all of IC were larger than 50 μm and were therefore undetected by the 2DC. These measurements were not included in the analysis of clear-sky RHi but were included in the analysis of overall RHi.

Tropopause Identification

While many of the RFs considered entered the lower stratosphere, measurements were included in this analysis only if the they were recorded in the troposphere. For each RF, the tropopause was identified as a persisting change in the lapse rate visible in the vertical profiles of the reference air temperature measurement. A unique tropopause height was identified for every ascent and descent in a given RF that appeared to cross the tropopause. Most DEEPWAVE RFs involved only one ascent and descent in the same location, so the two identified tropopause heights for each RF were usually very similar. ORCAS RFs also began and ended at the same location, but often involved multiple vertical transects throughout the flight at different latitudes, so the tropopause heights encountered varied somewhat. The HIPPO flights began and ended at different locations and involved multiple transects, so the tropopause heights varied significantly within individual flights. A case study of tropopause identification and UT data selection is shown in Figure 3. The lowest identified tropopause was at 7,760 km during DEEPWAVE RF17. The highest tropospheric altitude reached was 13,745 m during HIPPO-3 RF07, during which the aircraft did not appear to reach the tropopause.

2.2 CAM5

A comparison is made between the observations described above and CAM5, the latest version of Community Atmosphere Model (Neale et al., 2012). The model was run for five years with a horizontal resolution of 1.9° × 2.5° (latitude by longitude) and 30 pressure levels. The vertical resolution is about ~1,000 m at typical cirrus altitudes. CAM5 includes several updated

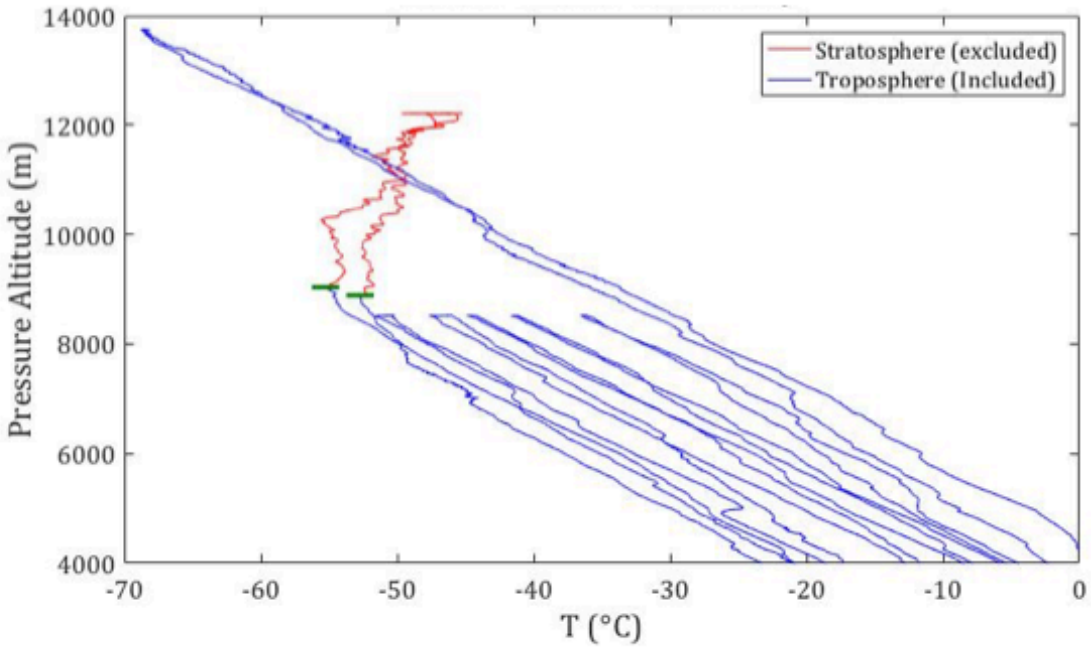

Figure 3. *Determination of tropopause height and selection of tropospheric data. The blue and red lines are temperature measurements from RF10 of HIPPO-5, which included several vertical transects and crossed the tropopause twice at similar altitudes (green dashes). Measurements from below the tropopause (blue) were included in this study, whereas stratospheric measurements (red) were not.*

components relative to previous versions, including a two-moment stratiform cloud microphysics scheme (Morrison and Gettelman, 2008) with ice microphysics modifications following Gettelman et al. (2010) and a cloud condensation parameterization that uses a new liquid cloud macrophysics closure described by Park et al. (2014). In this study, CAM5 has been supplemented with parameterizations of homogeneous and heterogeneous nucleation following Barahona and Nenes (2008) and Barahona and Nenes (2009). The model accounts for preexisting IC that are already present in a grid box before a separate nucleation event occurs, including IC form the previous timestep and detrained IC from convective clouds.

The aerosol treatment in CAM5 is the modal aerosol module with three modes (MAM3) as described by Liu et al. (2012). MAM3 simulates several different aerosol species, including sea salt, sulfate, primary and secondary organic matter, black carbon, and soil dust. The three modes are Aitken, accumulation, and coarse modes, and each has a prescribed lognormal size distribution. The module is capable of simulating internal mixing of species within modes and external mixing between modes. Both the mass mixing ratio of a single species and the total number concentration for all species can be predicted for a single mode. Since the aircraft

observations used in this study do not discriminate between aerosol species, this comparison will rely on total modal number concentration.

2.3 ECHAM-HAM

The second model used in this comparison is the general circulation model ECHAM6 (Stevens et al., 2013) coupled with the Hamburg Aerosol Module HAM2 (Zhang et al., 2012). The model was run for five years with a horizontal resolution of 1.86° × 1.875° (latitude by longitude) and 31 pressure levels. At typical cirrus altitudes, the vertical resolution is 700-800 m.

HAM2 simulates an aerosol ensemble of five species: sulfate, black carbon, particulate organic matter, sea salt, and mineral dust. Aerosol size distribution is represented by 7 lognormal modes: a single nucleation mode and soluble and insoluble Aitken, accumulation, and coarse modes. Like MAM3, it simulates internal mixing of species within aerosol modes and external mixing between modes. There are several improvements relative to the first version of the module, including: a two-moment stratiform cloud microphysics scheme (Lohmann et al., 2007); a new aerosol nucleation scheme (Kazil et al., 2010); aerosol water uptake for both non-organic and organic aerosols (O'Donnell et al., 2011; Petters and Kreidenweis, 2007); and explicit simulation of secondary organic aerosol (O'Donnell et al., 2011).

Both homogeneous and heterogeneous ice nucleation are considered during cirrus cloud formation in ECHAM6-HAM following Karcher et al. (2006) and the implementation by Kuebbeler et al. (2014). Homogenous nucleation is represented according to Koop et al. (2000) and heterogeneous nucleation can occur by deposition and immersion nucleation with accumulation and coarse mode dust IN. Like CAM5, the model accounts for preexisting and detrained IC.

2.4 Comparison

A general comparison was made between observations and model output. The parameters considered in this comparison and the methods by which they were retrieved from each data source are listed in Table 3**.** The comparisons were made by assessing vertical profiles of observations and model output. All aircraft observations were sorted by International Standard Atmosphere pressure altitude into 200-m bins, and statistics of the different parameters considered were calculated for each bin.

Table 3. Data sources for the comparison of observed and modeled parameters.

	Observations	CAM5	ECHAM-HAM
RHi	VCSEL and Reference Temperature*	One RHi field	Two RHi fields (in-cloud and clear-sky)
IC Number Conc.	2DC and CDP†	Cloud ice number conc.	Cloud ice number conc.
IC Size	2DC and CDP	N/A‡	N/A‡
Nucleation Mechanism	N/A	Fraction of new IC formed heterogeneously	Fraction of new IC formed heterogeneously
Total CN	Butanol CN Counter	Sum of aerosol modes	Sum of aerosol modes
Accumulation Mode Aerosols	UHSAS Total Conc. (0.06-1.0 μm)	Accum. mode number concentration ("A1")	Accum. mode number conc. (soluble+insoluble)

*See Formula **X** in Appendix for calculation.
†See Formula **X** in Appendix for calculation.
‡Only effective IC size was included in model output, which is not directly comparable to actual IC size.

Model output was retrieved as seasonal (DJF, MAM, JJA, SON) averages. For each model, four rectangular regions of the Southern Hemisphere were selected for comparison with aircraft observations. The first region is the smallest possible region that contain the full latitudinal and longitudinal range of the observations from all three aircraft campaigns. The second, third, and fourth regions encompass only the geographical ranges of DEEPWAVE, ORCAS, and HIPPO 1-5, respectively. For the comparisons of RHi and cloud microphysics, model output was averaged by pressure level over first region (red box in Figure 4) for each season of the 5-year model run. For each parameter, an annual regional average was calculated by taking the mean of the seasonal averages. The standard deviation of seasonal averages from the overall annual mean was also calculated. The midpoint pressure for each model pressure level was converted to pressure altitude for comparison with the average observations between all three campaigns. For aerosols, comparisons were made for separate geographic regions corresponding to individual aircraft campaigns. The same comparison procedure was followed

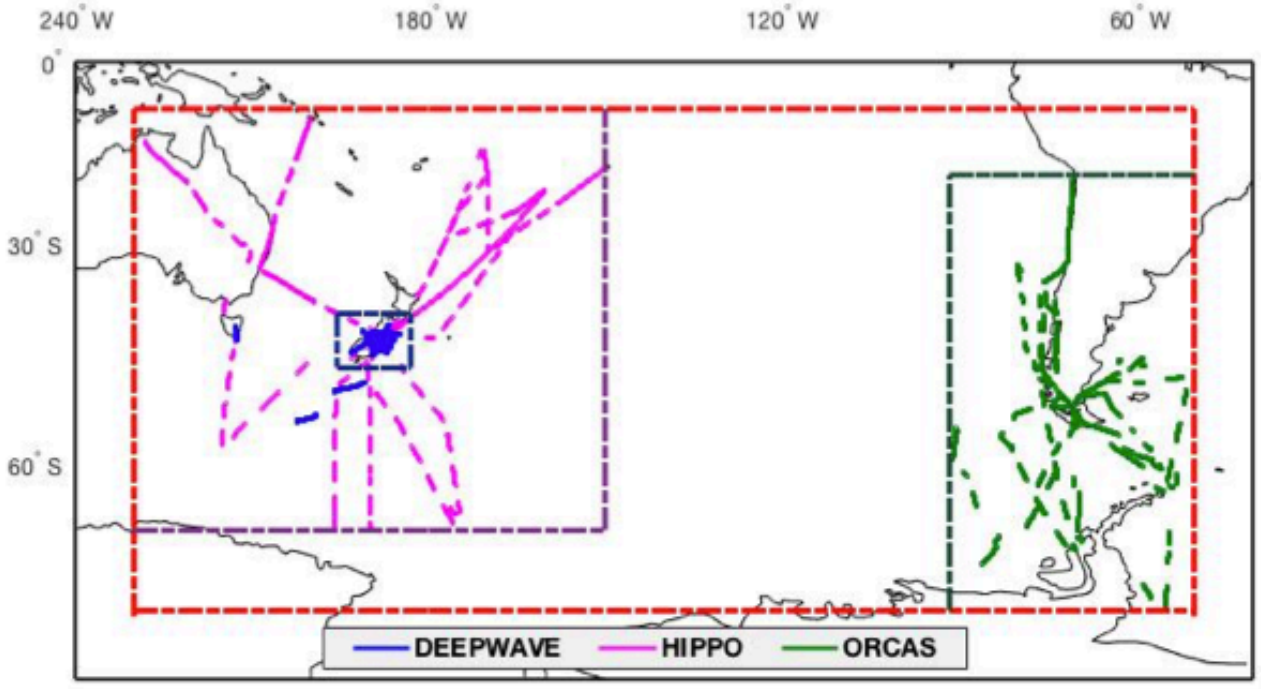

Figure 4. *Selection of model output for comparison to observations. Upper tropospheric measurements for each of the three campaigns are displayed as the scattered flight tracks. Stratospheric and lower tropospheric measurements are not shown. For RHi and microphysical comparisons, model output was averaged over the region encompassed by the red dashed lines. For aerosol comparisons with the individual campaigns, output was averaged over the rectangular regions corresponding to the campaign (DEEPWAVE: dark blue dashed lines; ORCAS: dark green; HIPPO: dark purple).*

for the smaller model output regions corresponding to each campaign. The seasonal variations of the different CAM5 and ECHAM-HAM parameters considered in this comparison are shown in the Appendix (8.2).

3 Results

3.1 Relative Humidity (RHi)

Altogether, about 50.9 hours of flight time were spent in the troposphere when T < -35°C. Approximately 32.8 and 2.5 of those hours were confidently classified as clear-sky and cirrus measurements, respectively. Ten of the hours were from DEEPWAVE and could not be classified as either clear-sky or cirrus measurements, and 5.5 hours were from HIPPO-1 when the CDP did not indicate the presence of a cloud but the measurements could not be confidently classified as clear-sky because of the absence of the 2DC.

In-Cloud

Of the 2.5 hours of recorded in-cloud measurements, 2.0 hours of RHi data were available. The distribution of in-cloud RHi and its variation with temperature are shown in Figure 5a. The mean and median in-cloud RHi for all T < -35°C were both 101%, which is very consistent with previous assessments of aircraft observations (Diao et al., 2014a; Krämer et al., 2009; Ovarlez et al., 2002; Wu et al., 2017). Approximately half of the measurements fell between 89% and 111% and 90% fell between 65% and 135%. Very few the measurements fell below 50%. As shown by the pink line on the right panel of Figure 5a, the average in-cloud RHi did not change significantly with decreasing temperature.

The distributions of RHi above ice saturation can be useful in inferring IC formation mechanisms (Haag et al., 2003). Apart from two outliers at 211% and 172%, the upper limit of the in-cloud RHi distribution was 164%. This is the same upper limit as that documented by Haag et al. (2003) for in-cloud conditions in the Southern Hemisphere using measurements from the INCA campaign. In this study, only 69 measurements (1.0%) exceeded 150%. The existence

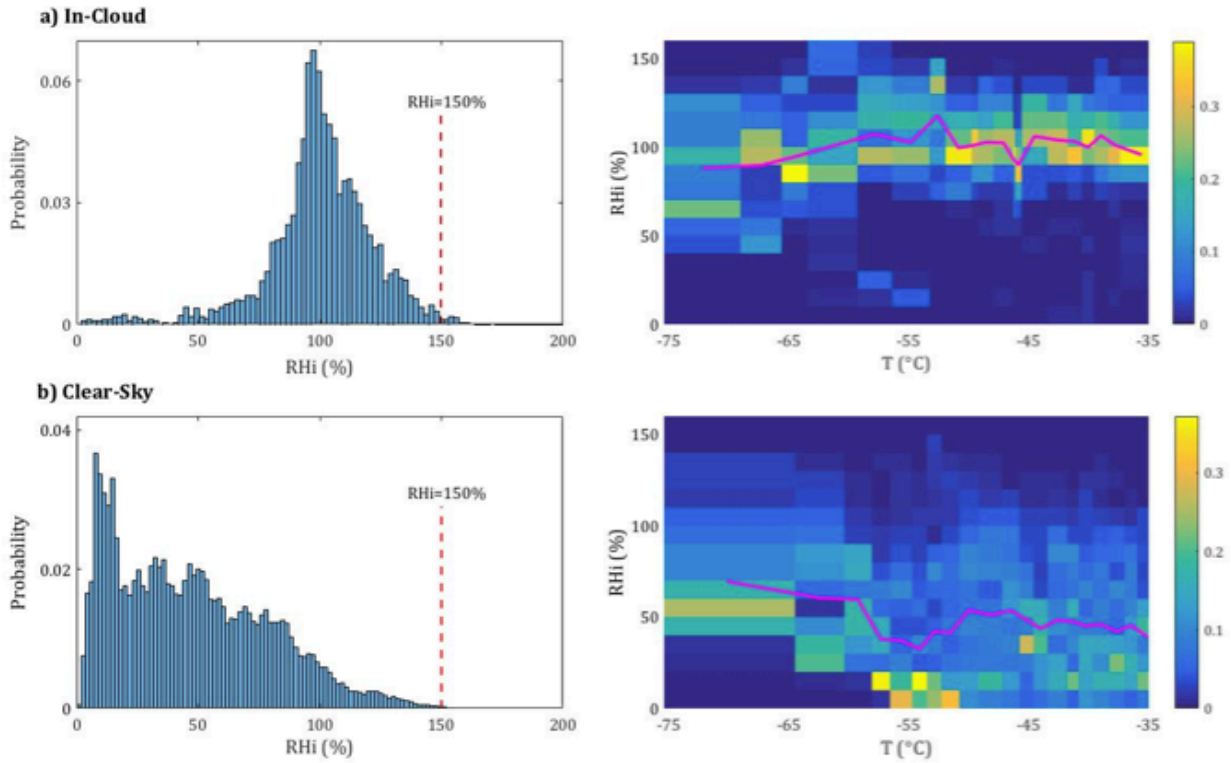

Figure 5. *Observed distributions of (a) in-cloud and (b) and clear-sky RHi. The left panels show a single probability distribution for all temperatures below -35°C. The right panels show the variation of the RHi distribution across the observed range of temperatures. Temperature bins are sized so that they all contain the same number of measurements. The sum of the frequency values (indicated by color shading) in each column is equal to 1. The pink lines represent the temperature-bin-averaged RHi.*

of these high measurements suggests that, at times, there are no IN available for heterogeneous nucleation and that homogeneous nucleation occurs. It is important to note that in-cloud RHi measurements less than 150% do not decisively indicate heterogeneous nucleation. Once ice nucleation occurs, IC grow at the expense of ambient water vapor and RHi decreases. Thus, RHi in a cloud that forms homogeneously can quickly drop well below the homogeneous nucleation threshold. Because the lifecycle stage of the observed cirrus clouds is not known, it is not possible to infer a nucleation mechanism for clouds with RHi < 150%. However, because RHi in a heterogeneously formed cloud would not increase after nucleation, it is safe to infer that homogeneous nucleation occurred when RHi is greater 150%. Additionally, in-cloud RHi above 140% also suggests a dearth of IN, since heterogeneous nucleation on dust IN typically occurs before RHi reaches 140% (Hoose and Möhler, 2012). Approximately 3.2% of measurements were above 140%.

Because there was no variable corresponding to in-cloud RHi in the CAM5 output, a comparison could only be made between the observed in-cloud RHi and that simulated by ECHAM-HAM. This comparison is shown in Figure 6 (left panel). ECHAM-HAM overestimates in-cloud RHi for the entire altitude range considered. Below 9,000 m, modeled RHi is about one standard deviation higher than the observations. At higher altitudes, modeled RHi is multiple standard deviations higher than the observations, reaching a maximum of 173%. Since this is an average value for a large geographic area, in-cloud RHi greater 173% was predicted for some grid boxes. Homogeneous nucleation occurs at about RHi ~150% when temperatures are sufficiently low. After nucleation, ambient RHi typically decreases as IC grow at the expense of the surrounding vapor. As such, RHi values greater than ~150% are extremely rare. This point is illustrated by the observed in-cloud RHi distribution (Figure 4, top left panel), in which the maximum RHi is 164% and RHi above 150% is very rare (1.0%). Thus, the very high in-cloud RHi predicted by ECHAM-HAM seems not just unlikely, but nearly unphysical.

Clear-Sky

Having assessed the distribution of RHi within cirrus clouds, RHi during clear-sky conditions is now considered. Of the 32.8 hours of measurements confidently classified as clear-sky, 31.5 hours of RHi data were available. The distribution of clear-sky RHi and its variation

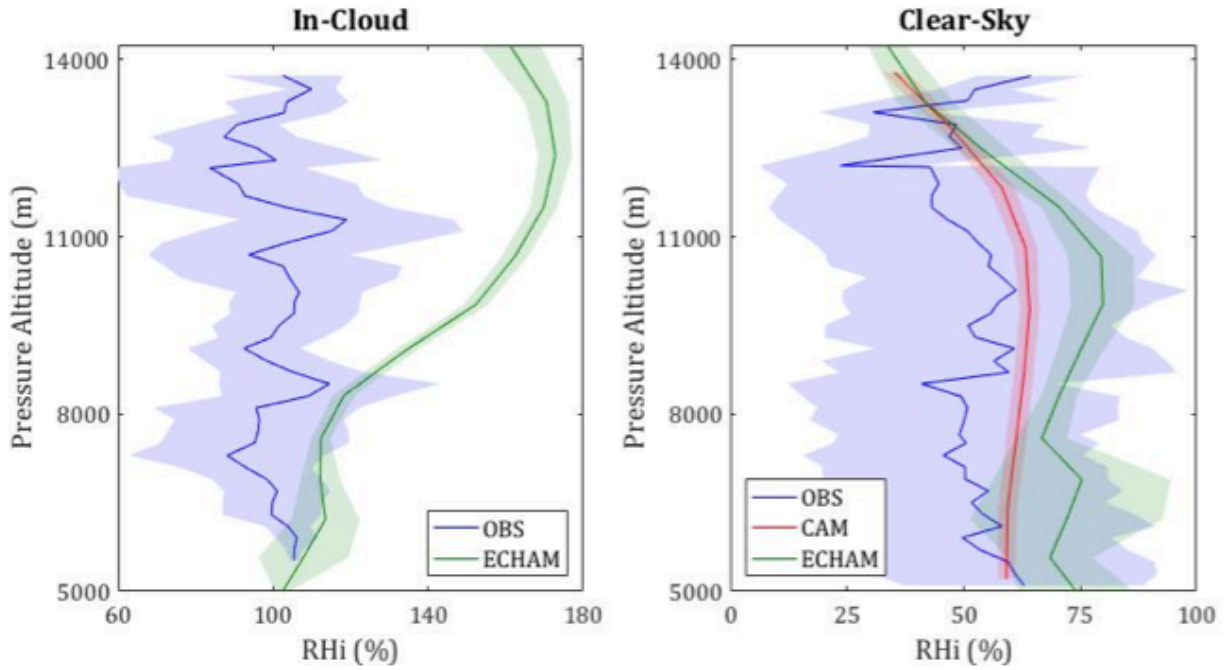

Figure 6. *Vertical profiles of modeled and observed in-cloud (left) and clear-sky (right) RHi. Observations are grouped into 200-m altitude bins. The shaded areas extend for one standard deviation above and below the average. For the models, the shaded standard deviation is the standard deviation of individual seasonal averages from the overall annual average. There was no CAM5 variable corresponding to in-cloud RHi*

with temperature are shown in Figure 5b. The mean and median clear-sky RHi for all T < -35°C were 47% and 43%, respectively. Approximately one-quarter of the measurements fell below 20%, two-thirds fell between 20% and 100%, and 6% exceeded 100%. There is no evident temperature trend for clear-sky RHi.

The upper limit of the clear-sky distribution was 174%, which is higher than the upper limit of the in-cloud distribution and 18% higher than the upper limit of the INCA clear-sky distribution reported by Haag et al. (2003). It is reasonable that the observed upper limit of clear-sky RHi is higher than that of in-cloud RHi, since RHi should only decrease after ice nucleation. In this study, only 399 (0.4%) clear-sky measurements fell above 140% and only 112 (0.1%) measurements fell above 150%. Measurements between 140% and 150% suggests that IN were sparse if not completely absent, whereas measurements greater than 150% indicate the complete absence of IN and, therefore, that homogeneous nucleation is possible.

The comparison between observed, CAM5, and ECHAM-HAM clear-sky RHi is shown in Figure 6 (right panel). It is important to note that the CAM5 run used in this comparison provided a single RHi variable for each grid box. This variable includes both in-cloud and clear-

sky conditions, and so its comparison to observed in-cloud RHi must be taken with caution. RHi predicted by CAM5 is typically only slightly higher than the observations, falling well within one standard deviation. Given that the CAM5 RHi includes in-cloud conditions and should therefore be skewed higher than true clear-sky RHi, it is reasonable to conclude that CAM5 simulates clear-sky RHi with high accuracy. ECHAM-HAM generally overestimates clear-sky RHi with respect to the observations but typically falls within one standard deviation. Both CAM5 and ECHAM-HAM predict a relative RHi peak at ~10,000 m. At ~13,000 m, both models predict RHi very similar to observed values. At higher altitudes, the models underestimate RHi. It is possible that at these high altitudes, a fair number of the model grid boxes actually lie above the modeled tropopause and are thus very dry, whereas all of the observational measurements considered fall below the tropopause. Thus, the inclusion of some modeled stratospheric grid boxes in this comparison may explain the models' underestimate of RHi.

Combined RHi

In order to better evaluate the single CAM5 RHi variable and to include the 11.2 hours of RHi measurements for which cloudiness was indeterminable, total RHi irrespective of cloud conditions was assessed. In total, there were 44.9 hours of RHi measurements for which T < -35°C across the three aircraft campaigns. Approximately 75% (33.5 hours) of these measurements are the in-cloud and clear-sky measurements examined previously; 22% (10.1 hours) are DEEPWAVE measurements that, according to RICE, did not occur in the presence of supercooled water; 3**%** (1.4 hours) are HIPPO-1 measurements that showed no indication of cloudiness from RICE or CDP but which could not be confidently labeled as clear-sky due to the absence of the 2DC. The overall RHi distribution and its variation with temperature are shown in Figure 7. The mean and median RHi for these measurements were 52% and 48%, respectively. RHi falls below 50% in just over half of the measurements, and ice supersaturation occurs 10% of the time. Again, RHi above 140% and 150% is extremely rare (0.8% and 0.3%, respectively). While average RHi for -75°C < T < -65°C is significantly higher than RHi at warmer temperatures, there is no general temperature trend for T > -65°C.

The comparison between observed, CAM5, and ECHAM-HAM total RHi is shown in Figure 8**.** CAM5 predicts total RHi with relatively high accuracy over a large altitude range.

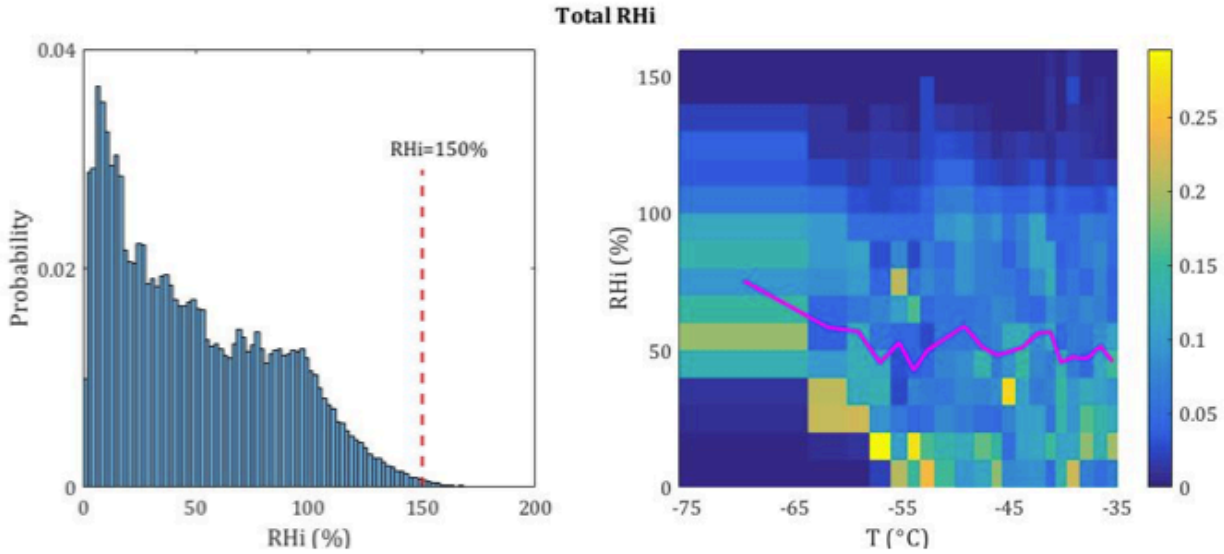

***Figure** 7. Probability distribution (left) and temperature variation (right) of aggregated RHi for all three campaigns, irrespective of cloud condition. The pink line on the right panel represents the temperature-bin-averaged RHi. Shading color indicates probability.*

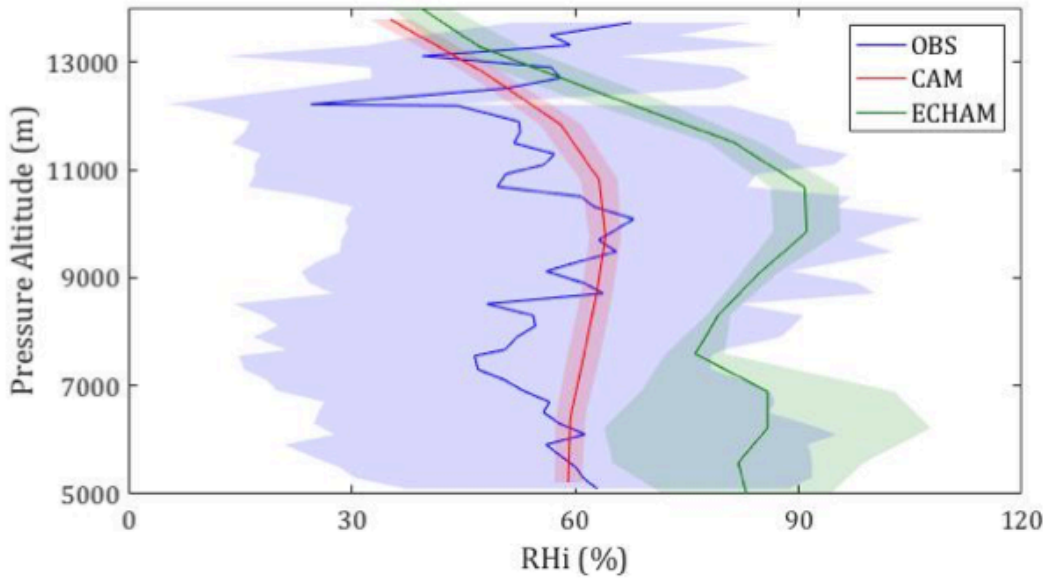

***Figure 8.** Comparison of modeled and observed overall RHi irrespective of cloud conditions with overall model RHi.*

ECHAM-HAM, consistently higher than CAM5, generally overestimates RHi by about one standard deviation. Again, both models predict a RHi maximum at ~10,000 m, corresponding well to the observed maximum at ~10,100 m. However, while the CAM5-predicted maximum average RHi of 64% is close to the observed maximum of 68%, the maximum predicted by ECHAM-HAM is much higher at 91%.

3.2 Cloud Microphysics

Both CDP and 2DC measurements were available for 1.8 of the 2.5 hours of recorded in-cloud measurements. The remaining 0.7 hours of measurements include measurements from only one of the instruments and are excluded from the analysis of cloud microphysics due to limited particle detection range. Of the 1.8 hours for which there are CDP and 2DC measurements, readings from both of the instruments are nonzero only 37% of the time (0.66 hours). CDP measurements were equal to zero 44% of the time, during which the surrounding cirrus cloud consisted of only IC larger than 50 μm. On the other hand, 2DC measurements were equal to zero 19% of the time, during which only particles smaller than 62 μm were present.

The distribution of in-cloud IC number concentration (N_i) for T < -35°C based on the 1.8 hours of combined measurements is shown in Figure 9 (left panel)**.** The magnitude of N_i spans six orders of magnitude, from 0.026 L^{-1} to 10,016 L^{-1}. The overall mean and median in this assessment are 116 L^{-1} and 18 L^{-1}, respectively. For the 44% of measurements when the CDP concentration was zero, the mean and median were 7.3 L^{-1} and 3.8 L^{-1}, respectively. For the 19% of measurements when the 2DC concentration was zero, the mean and median were 139 L^{-1} and 19.6 L^{-1}, respectively. There is no apparent trend in mean or median N_i with temperature, as

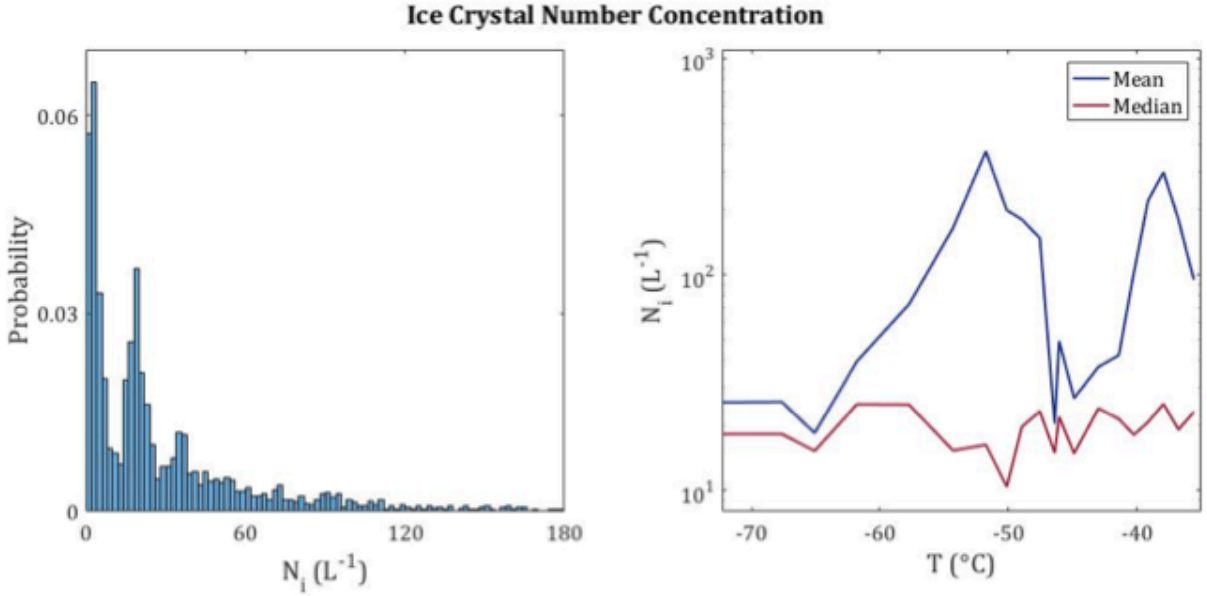

Figure 9. *Probability distribution (left) and temperature variation (right) of observed ice crystal number concentration. Note that N_i greater than 180 L^{-1} were observed, but not with great enough frequency for them to be visible in the distribution plot. In the panel on the right, mean (blue line) and median (red line) N_i were calculated for temperature bins that all contained the same number of measurements.*

shown in the right panel of Figure 9**.** The typical N_i observed here (red line, right panel of Figure 9) has the same magnitude as that found by Krämer et al. (2009) over the same temperature range, but is generally lower than what was detected in cirrus clouds around Australia by (Gallagher et al., 2005), who observed a N_i distribution with a mode between 10^2 and 10^3 L^{-1}. However, average N_i in this study is generally higher and has a wider range than documented by Wu et al. (2017) for HIPPO 2-5, which is likely because that study assessed N_i only for IC larger than 75 μm whereas this study considers smaller IC as well.

Nearly 90% of N_i observations fall below 100 L^{-1}. This low N_i is suggestive of heterogeneous nucleation, and its high frequency of occurrence in these observations suggests that heterogeneous nucleation was responsible for the formation of most of the cirrus clouds encountered during these aircraft campaigns. However, the presence of clouds with N_i in the 10^2-10^3 L^{-1} indicates that homogeneous nucleation also occurred. Thus, it is likely that both heterogeneous and homogeneous nucleation played a role in the formation of the observed cirrus clouds.

Mean IC diameter (D_{mean}) was also recorded by the 2DC and CDP. The distribution of in-cloud D_{mean} for T < -35°C based on the 1.8 hours of combined measurements is shown in Figure 9 (left panel)**.** D_{mean} ranged from 2.4 μm to 2.1 mm with an average of 138 μm. When the CDP measurements were zero and only large IC were present, D_{mean} was 246 μm. When 2DC

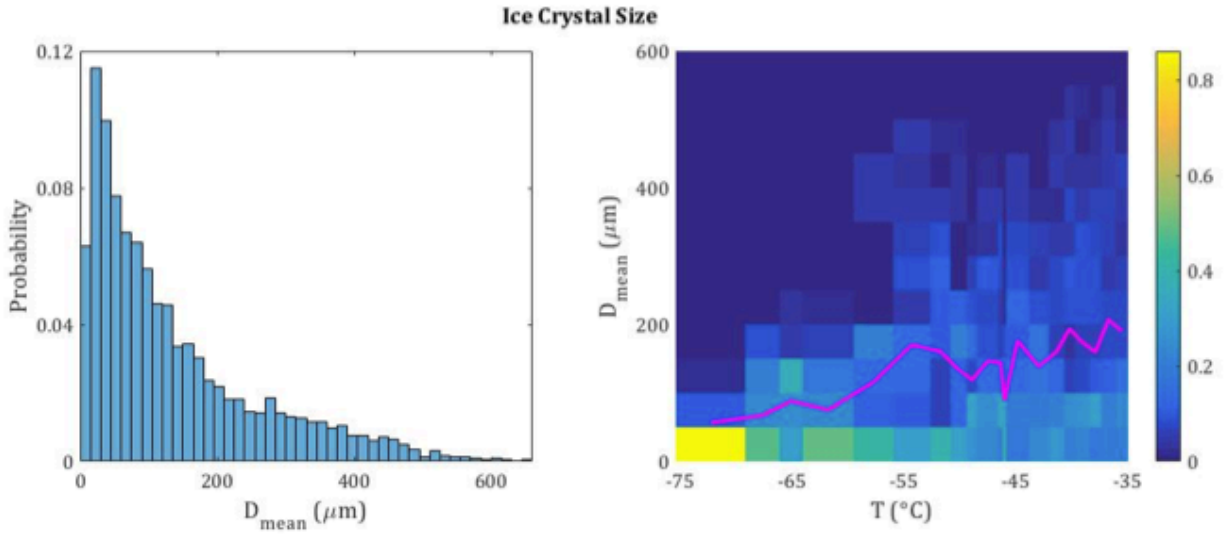

Figure 9. *Probability distribution (left) and temperature variation (right) of observed average ice crystal diameter. The pink line represents the temperature-bin-averaged average ice crystal diameter. Shading color indicates probability.*

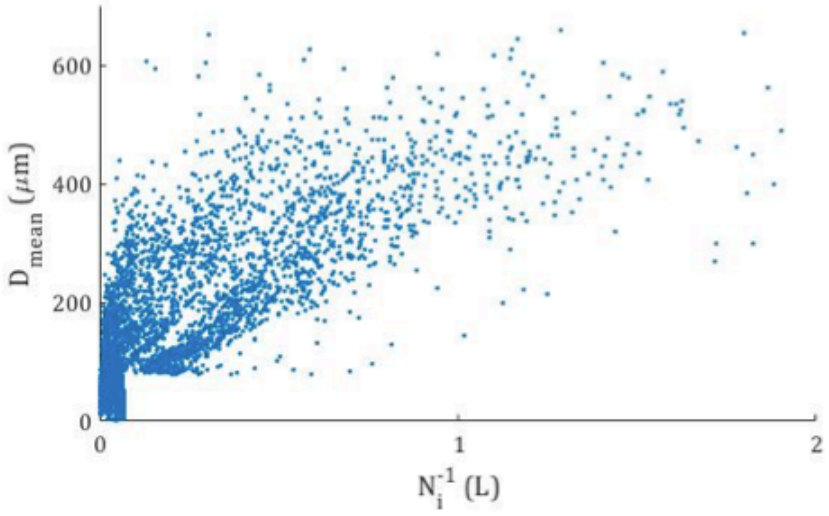

Figure 10. *Observed relationship between the inverse of N_i (x-axis) and the mean IC diameter (y-axis). Each point represents one measurement.*

measurements were zero and only small IC were present, D_{mean} was 21 μm. IC size generally decreased as temperature decreased, as is shown by the pink line in the right panel of Figure 9. This trend is consistent with previous analyses of aircraft IC observations (Eidhammer et al., 2014; Wu et al., 2017). IC size is inversely related to N_i (Figure 10), as has been the case in previous analyses in the Southern Hemisphere (Gallagher et al., 2005). This suggests that IC are either present in high concentrations of small IC or low concentrations of large IC.

A comparison of modeled and observed N_i is shown in Figure 11**.** A comparison of observed and modeled D_{mean} is not included in this study because the model output only included *effective* IC size, which is not directly comparable to actual IC size. CAM5 greatly overestimates N_i by one to two orders of magnitude throughout the entire altitude range considered. The pressure-level-averaged N_i predicted by CAM5 ranges from 1467 L^{-1} at the highest altitude considered to 4875 L^{-1} at 8,700 m. Only 2.0% of the N_i observations exceed the minimum CAM5 pressure level average, suggesting that N_i predicted by CAM5 is a very large overestimate. ECHAM-HAM predicts significantly lower N_i than CAM5 but still exceeds observations by around one order of magnitude at altitudes below 8,000 m. However, at higher altitudes, ECHAM-HAM predictions closely match N_i observations. Pressure-level-averaged N_i predicted by ECHAM-HAM ranges from 41 L^{-1} at 12,400 m to 922 L^{-1} at 7,600 m.

Ice crystal detrainment is a likely explanation for the overestimation of N_i by both CAM5 and ECHAM-HAM. In CAM5, IC detrained from deep convection have an initial crystal size of

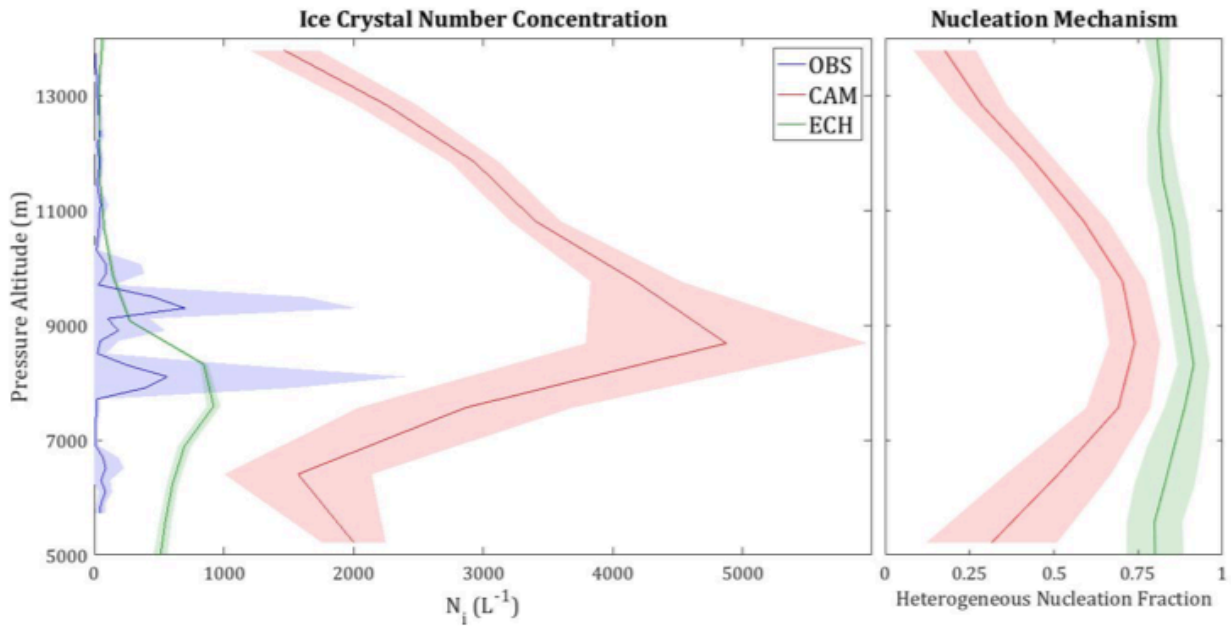

Figure 11. *Comparison of modeled and observed N_i (left); fraction of modeled ice nucleation that occurs heterogeneously (right).*

10 μm (Zhang et al., 2013). Only 5% of D_{mean} observations fell below 10 μm, which suggests that CAM5 underestimates the size of detrained IC. Because small IC size typically corresponds to high N_i, detrainment could bear significant responsibility for the extreme overestimation of N_i in CAM5. Detrained IC in ECHAM-HAM are initially larger than those in CAM5 (Kuebbeler et al., 2014). As a result, the overestimate of N_i is more modest than in CAM5. It is possible that the altitudes at which maximum N_i occurs (8,700 m in CAM5 and 7,600 m in ECHAM-HAM) correspond to the maximum level of detrainment from deep convection.

At this point in the discussion of modeled cirrus microphysics, it is useful to consider the relative importance of homogeneous and heterogeneous nucleation in the two simulations. The fraction of ice nucleation that occurs heterogeneously is shown in the right panel of Figure 11**.** Heterogeneous nucleation consistently dominates in ECHAM-HAM, with the heterogeneous fraction remaining above 0.75 across the entire altitude range considered. In CAM5, there is more homogeneous nucleation and more general variability in nucleation mechanism. Heterogeneous nucleation dominates between 6,500 m and 11,500 m, though not to the extent to which it dominates in ECHAM-HAM, and homogeneous nucleation dominates outside of this altitude range. In both simulations, high heterogeneous nucleation fraction corresponds to high N_i, which is the opposite of what would be expected, since heterogeneous nucleation typically results in low

N_i. It is clear that the treatment of detrained IC in both models prevents an isolated examination of the relationship between ice nucleation mechanism and cirrus microphysical properties.

3.2 Aerosols

Condensation Nuclei

Altogether, there were 36.6 hours of CN concentration measurements recorded by the butanol CN counter, 14.3 of which were from DEEPWAVE and 22.3 of which were from ORCAS. There are no CN measurements for HIPPO 1-5 because the butanol CN counter was not on board. Average CN number concentrations for DEEPWAVE and ORCAS are shown in Figure 12a**.** The two aircraft campaigns are displayed separately to highlight the significant observational differences between two campaigns, which were not present for the parameters discussed thus far. Total CN concentrations were significantly higher during ORCAS than during DEEPWAVE, often by a factor of three or more. For both campaigns, CN concentration generally decreases with altitude.

Because of the differences in CN concentrations between DEEPWAVE and ORCAS, individual comparisons were made between each campaign and the geographically corresponding modeled region. The comparison of observed and modeled CN concentrations in the region corresponding to DEEPWAVE (dark blue box in Figure 4) is shown in Figure 13a. Concentrations predicted by CAM5 agreed well with observations at higher altitudes but were generally lower than observations at altitudes below 9,000 m, often by a factor of 2. ECHAM-HAM CN concentrations, consistently higher than those from CAM5, agreed well with observations at lower altitudes but were slightly higher at high altitudes. The comparison for the region corresponding to ORCAS (dark green box in Figure 4) is shown in Figure 13b. Both models underestimated CN concentrations at all altitudes, often by a factor of 2 or more. Again, ECHAM-HAM concentrations were consistently higher than those predicted by CAM5. It is worth noting that both models correctly predicted higher CN concentrations in the ORCAS region than in the DEEPWAVE region, though the magnitude of this difference was underestimated. Furthermore, in both regions, CAM5 does not predict the observed decrease in CN with altitude. In fact, CAM5 predicts about twice as many CN at ~10,000 m as it does at ~5,000-6,000 m in the DEEPWAVE region, though the average concentration begins to fall at altitudes higher than 10,000 m.

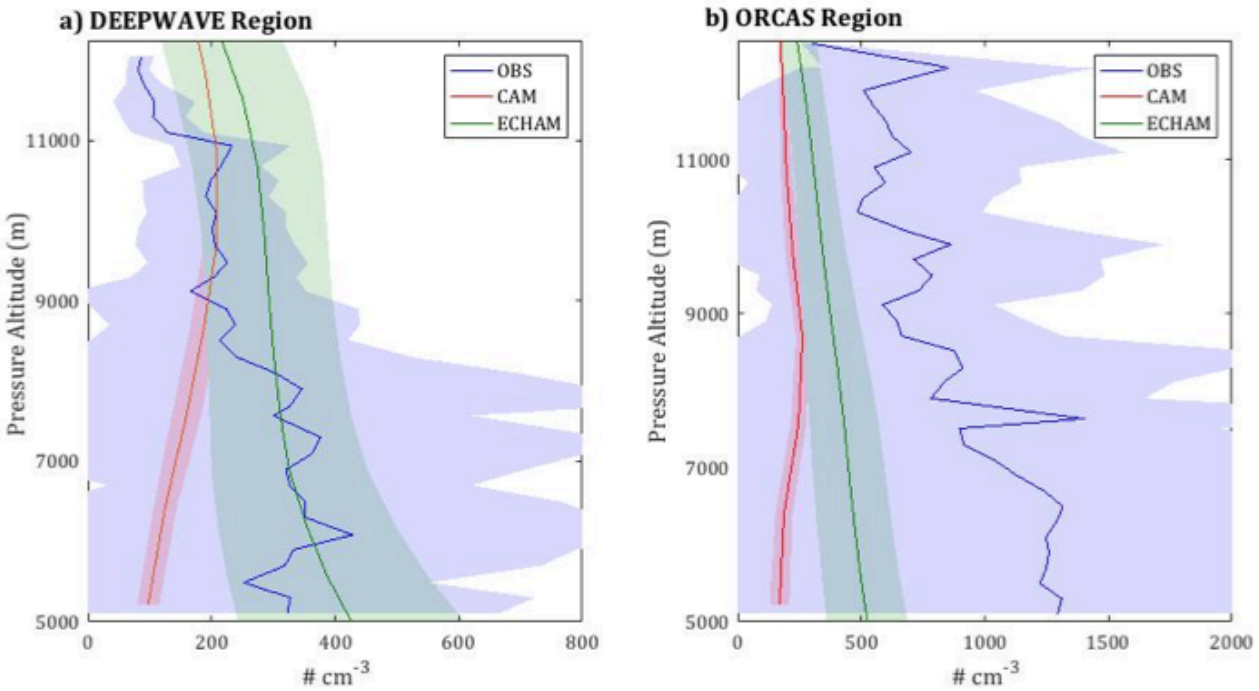

Figure 13. *Comparison of modeled and observed CN concentration for the geographic regions corresponding to (2) DEEPWAVE and (b) ORCAS.*

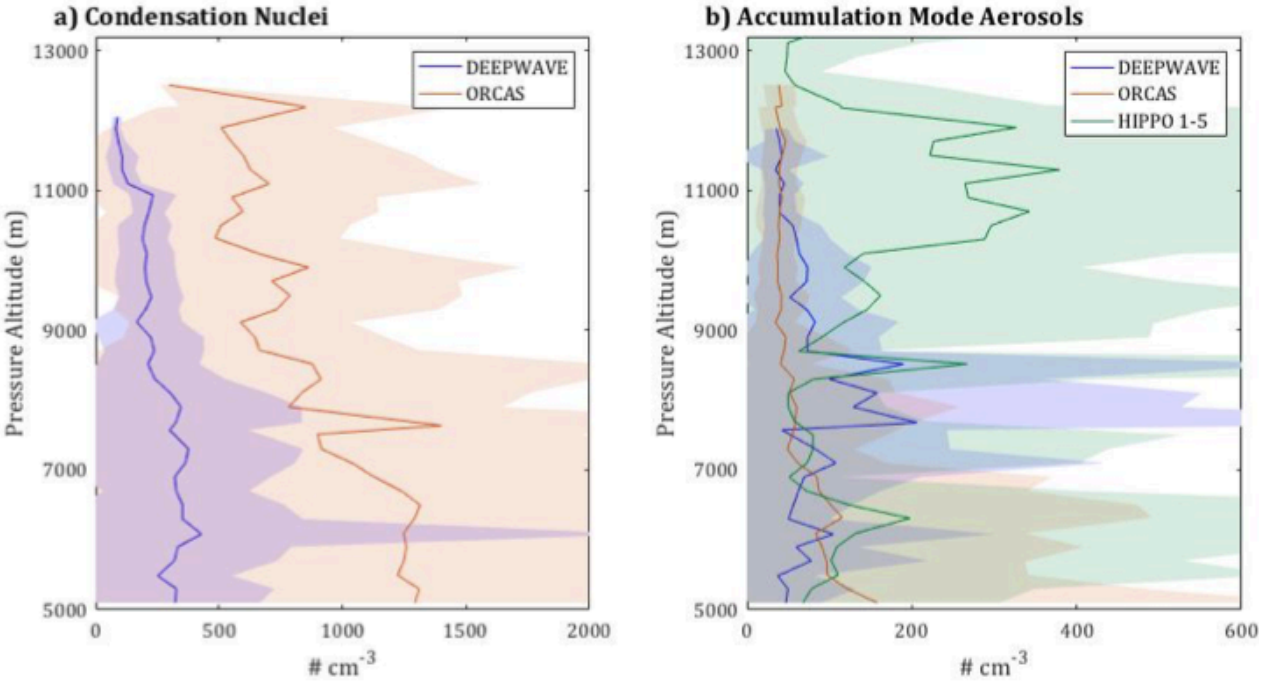

Figure 12. *Vertical profiles of observed (a) CN concentrations during DEEPWAVE (blue) and ORCAS (orange) and (b) accumulation mode aerosol concentrations during DEEPWAVE (blue), ORCAS (orange), and HIPPO 1-5 (green). Concentrations are average by 200-m altitude bin.*

Accumulation Mode Aerosols

Between the three campaigns, there were 56.8 hours of accumulation mode aerosol (0.06-0.10 μm) measurements from the UHSAS. Average number concentrations of accumulation mode aerosols (AMA) for the three campaigns are shown in Figure 12b. Average AMA concentrations during ORCAS decrease with altitude, but there was no trend in AMA during DEEPWAVE and HIPPO 1-5. Unlike CN, AMA concentrations were similar across the different campaigns with the exception of anomalously high concentrations during DEEPWAVE between 7,600 m and 8,600 m and during HIPPO above 9,000 m. The DEEPWAVE anomaly between 7,600 m and 8,600 m is due to the especially high concentrations encountered during RF05 and RF20. Concentrations during these two flights were, at times, an order of magnitude higher than the concentrations encountered in the same altitude range during other DEEPWAVE RFs, which were typically similar to average concentrations at other altitudes. Similarly, the HIPPO anomaly at altitudes above 9,000 m is caused by very high AMA concentrations encountered during a single RF (HIPPO-3 RF07). For all other HIPPO flights, concentrations were much closer to those encountered during DEEPWAVE and ORCAS.

The comparison of modeled and observed AMA concentrations in the DEEPWAVE region is shown in Figure 14a. Apart from the anomaly in observations between 7,600 m and 8,600 m, modeled AMA concentrations are relatively accurate. For the ORCAS region (Figure 14b), both models accurately predicted AMA at higher altitudes but underestimated AMA at altitudes below 9,000 m, often by a factor of four to five. In the region corresponding to HIPPO 1-5 (dark purple box in Figure 4), modeled AMA concentrations were consistently lower than observations, with the exception of high CAM5 accuracy at altitudes above 12,500 m (Figure 14c). The discrepancy between the models and observations was largest between 10,000 m and 12,200 m, over which observed AMA were anomalously high. In all three regions, ECHAM-HAM predicts more AMA than CAM5 at lower altitudes but less at higher altitudes, though the altitude at which this switch occurs varies slightly between the regions. Again, CAM5 predicts that average AMA concentration slightly increases with height, whereas ECHAM-HAM predicts a slight decrease.

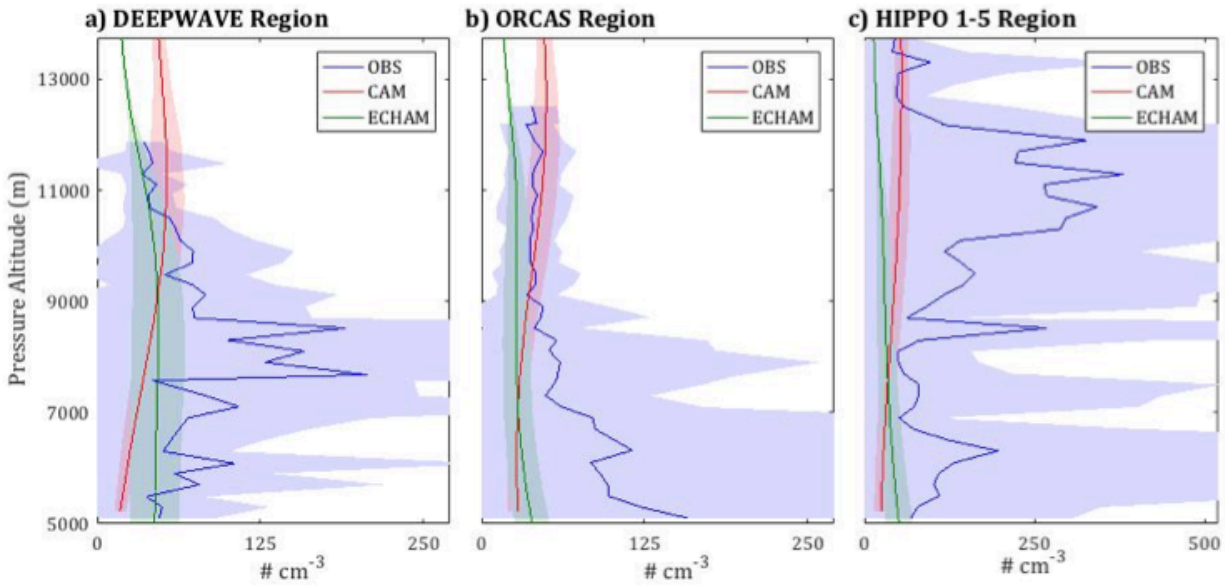

Figure 14. *Comparison of modeled and observed accumulation mode aerosol concentrations for the geographic regions corresponding to (a) DEEPWAVE, (b) ORCAS, and (c) HIPPO 1-5.*

4 Discussion

The aircraft observations of RHi and cirrus cloud microphysics examined in this study suggest that both homogeneous and heterogeneous ice nucleation occur in the Southern Hemisphere. These findings challenge the belief that homogeneous nucleation dominates in the Southern Hemisphere (Gallagher et al., 2005; Haag et al., 2003; Mitchell and Finnegan, 2009) and are consistent with recent studies that underscore the global relevance of heterogeneous nucleation (Cziczo et al., 2013). The N_i distribution observed in this study is heavily skewed towards low values that are indicative of heterogeneous nucleation. However, a small but notable number of observations reveal high RHi and N_i inside of some cirrus clouds, indicating that while homogeneous nucleation may not completely dominate in the Southern Hemisphere, it certainly plays a role in cirrus cloud formation.

The model comparison presented here reveals the relative strengths and weaknesses of ECHAM-HAM and CAM5. In ECHAM-HAM, in-cloud RHi is predicted to be very high despite the general dominance of heterogeneous nucleation. It is difficult to reconcile the model's prediction of RHi exceeding 150% and a heterogeneous formation fraction of ~80% in the same altitude range. These results call into question the microphysics scheme developed by Karcher et al. (2006) and implementation by Kuebbeler et al. (2014).

Both models overestimate N_i, though ECHAM-HAM to a much lesser extent and only at lower altitudes. Because IC detrainment is likely responsible for a substantial part of this bias, it cannot be concluded that the overestimation of N_i stems from a model bias towards homogeneous nucleation. However, it is fair to conclude that N_i is greatly misrepresented in CAM5, whether due to detrainment or otherwise. A detailed decomposition of model N_i biases could reveal the relative responsibility of detrained IC and ice nucleation mechanism in creating and influencing the magnitude of this bias. Furthermore, model treatments of detrained IC must be reassessed so that modeled N_i falls within the observational range.

In general, both models slightly underestimated the concentration of accumulation mode aerosols (0.06-0.10 μm). Since IN in the upper troposphere typically fall into this size range, the models could be underestimating the availability of IN and, in turn, the relative importance of heterogeneous nucleation. For CAM5, the aerosol bias correction could have substantial impacts on cirrus cloud properties, since the model simulates a significant amount of homogeneous nucleation. Since ECHAM-HAM already predicts that heterogeneous nucleation dominates, the correction of the aerosol bias would diminish the importance of homogeneous nucleation even further.

This study has several limitations. Firstly, this comparison relies on a limited amount of in-cloud aircraft measurements (~2 hours cumulatively across the campaigns). Because the data is limited, observed averages could be substantially influenced by specific meteorology. On the other hand, the model output that was averaged both over large individual grid boxes and over a very large geographic region, and the models were not forced with meteorology corresponding to the time of the individual research flights. Thus, the comparisons presented here must be interpreted with caution. In order to make more robust comparisons, more in situ measurements of cirrus clouds in the Southern Hemisphere are urgently needed.

Secondly, there is considerable uncertainty in the observations of cloud microphysics used in this comparison. In order to estimate N_i, number concentration measurements from two separate instruments were combined, and there was a small gap in the range of detectable particle sizes (50-62 μm). For 63% of the measurements, one of the two instruments (CDP or 2DC) measured an IC number concentration of zero. While it is certainly possible that some cirrus clouds contain only IC larger than 50 μm or only smaller than 62 μm, more confidence in the

microphysics would be gained if N_i were measured by a single instrument that could detect a broad range of particle sizes.

Despite its limitations, this study reveals several significant discrepancies in observed and modeled parameters. These findings illuminate the need for further improvement of GCM microphysics schemes. Furthermore, the observations considered in this study underscore the importance of heterogeneous nucleation in the Southern Hemisphere and emphasize the need for a greater understanding of hemispheric differences in cirrus cloud properties.

5. Summary

A summary of model performance with respect to observations from the DEEPWAVE, ORCAS, and HIPPO 1-5 campaigns is presented in Table 4. In-cloud observations reveal that RHi can approach and sometimes exceed the homogeneous nucleation threshold, indicating that homogeneous nucleation does occur in the upper troposphere of the Southern Hemisphere. However, observed ice crystal number concentrations were lower than the concentrations typical of homogeneous nucleation, suggesting that heterogeneous nucleation likely plays a substantial role in cirrus formation. This study does *not* suggest that heterogeneous nucleation is the dominant, or even the more common, mechanism of ice nucleation; rather, it simply highlights the need to reevaluate the assumption that almost all cirrus cloud formation in the Southern Hemisphere occurs homogeneously. These results highlight the need for more in situ observations of cirrus clouds in the Southern Hemisphere.

The importance of heterogeneous nucleation is further demonstrated by the ECHAM-HAM simulation, which predicts that over 70% of IC form heterogeneously. However, despite the prominence of heterogeneous nucleation, the model predicts in-cloud RHi that, on average, far exceeds the homogeneous nucleation threshold. This inconsistency casts ample doubt on the cirrus cloud parameterizations used in the model. On the other hand, the high accuracy of RHi simulated by CAM5 suggests that the CAM5 parameterizations may better reflect actual cirrus cloud properties. CAM5 predicts a more equal balance between homogeneous and heterogeneous nucleation that shifts with altitude.

Both models overestimate observed cirrus N_i. ECHAM-HAM overestimates N_i by an order of magnitude at altitudes below 8,000 m but is very accurate at higher altitudes, whereas CAM5 consistently overestimates N_i by one to two orders of magnitude. In each model, the

Table 4. Summary of model performance with respect to observations.

	CAM5	ECHAM-HAM
In-Cloud RHi	N/A	Moderate overestimate below 8 km; Large overestimate above 8 km.
Clear-Sky RHi	Accurate.	Modest overestimate.
N_i	Very large overestimate.	Large overestimate below 8 km; Accurate above 8 km.
Total CN	Moderate underestimate in DEEPWAVE region below 8,000 m, accurate above 8,000 m; Large underestimate in ORCAS region.	Accurate in DEEPWAVE region; Large underestimate in ORCAS region.
Accum. Mode Aerosols	Accurate in DEEPWAVE region; Moderate underestimate in ORCAS region below 9 km, accurate above 9 km; Slight underestimate below 12 km in HIPPO region, accurate above 12 km.	Accurate in DEEPWAVE region; Moderate underestimate in ORCAS region; Slight underestimate in HIPPO region.

largest overestimation occurs in the same altitude range as the maximum heterogeneous nucleation fraction. Because a high heterogeneous nucleation fraction should correspond to low N_i, it is clear that there are other factors besides nucleation mechanism that govern modeled N_i. One of these factors is detrained IC, which are likely being represented as too small and in too high a concentration. Improvements must be made to model treatment of detrained and other preexisting IC so that modeled N_i more accurately reflects observations.

The comparison of observed and modeled aerosol concentrations illuminates some modest model biases. Both models fail to replicate the geographic variation in CN concentration revealed by the comparison of DEEPWAVE and ORCAS observations. Modeled accumulation mode aerosol concentrations vary from highly accurate to significantly underestimated. Given that the chemical characteristics, availability, and behavior of IN are poorly understood, any causal relationship that exists between model aerosol biases and simulated cirrus cloud properties is not immediately clear.

6. Acknowledgements

I would like to thank my thesis advisor Trude Storelvmo for the very valuable guidance and expertise she has provided over the last two years. Professor Storelvmo's mentorship has been an integral part of the development of my academic passions and research interests, and I am grateful for the opportunity she gave me to join her research group when I was just an underclassman with no research experience. I greatly appreciate all of the time she devoted to supporting this project.

I would also like to thank Ron Smith, my second reader, whose teaching is what first drew me to the atmospheric sciences. I am grateful for the many valuable insights he has provided and the time he spent helping me interpret the aircraft datasets used in this study. This project would not have been possible without his help.

I thank Blaz Gasparini of the Institute for Atmospheric and Climate Science at ETH Zurich and Jørgen Jensen of NCAR for their very generous assistance with this project.

7. References Cited

Barahona, D., and Nenes, A., 2008, Parameterization of cirrus cloud formation in large-scale models: Homogeneous nucleation: Journal of Geophysical Research, v. 113, no. D11.

Barahona, D., and Nenes, A., 2009, Parameterizing the competition between homogeneous and heterogeneous freezing in ice cloud formation - polydisperse ice nuclei: Atmospheric Chemistry and Physics, v. 9, no. 16, p. 5933-5948.

Cober, S. G., Isaac, G. A., and Korolev, A. V., 2001, Assessing the Rosemount Icing Detector with in situ measurements: Journal of Atmospheric and Oceanic Technology, v. 18, no. 4, p. 515-528.

Cziczo, D. J., Froyd, K. D., Hoose, C., Jensen, E. J., Diao, M. H., Zondlo, M. A., Smith, J. B., Twohy, C. H., and Murphy, D. M., 2013, Clarifying the Dominant Sources and Mechanisms of Cirrus Cloud Formation: Science, v. 340, no. 6138, p. 1320-1324.

Diao, M., Zondlo, M. A., Heymsfield, A. J., Avallone, L. M., Paige, M. E., Beaton, S. P., Campos, T., and Rogers, D. C., 2014a, Cloud-scale ice-supersaturated regions spatially correlate with high water vapor heterogeneities: Atmos. Chem. Phys., v. 14, no. 5, p. 2639-2656.

Diao, M., Zondlo, M. A., Heymsfield, A. J., and Beaton, S. P., 2014b, Hemispheric comparison of cirrus cloud evolution using in situ measurements in HIAPER Pole-to-Pole Observations: Geophysical Research Letters, v. 41, no. 11, p. 4090-4099.

Dufresne, J. L., and Bony, S., 2008, An assessment of the primary sources of spread of global warming estimates from coupled atmosphere-ocean models: Journal of Climate, v. 21, no. 19, p. 5135-5144.

Eidhammer, T., Morrison, H., Bansemer, A., Gettelman, A., and Heymsfield, A. J., 2014, Comparison of ice cloud properties simulated by the Community Atmosphere Model (CAM5) with in-situ observations: Atmospheric Chemistry and Physics, v. 14, no. 18, p. 10103-10118.

Field, P. R., Heymsfield, A. J., and Bansemer, A., 2006, Shattering and particle interarrival times measured by optical array probes in ice clouds: Journal of Atmospheric and Oceanic Technology, v. 23, no. 10, p. 1357-1371.

Fritts, D. C., Smith, R. B., Taylor, M. J., Doyle, J. D., Eckermann, S. D., Dornbrack, A., Rapp, M., Williams, B. P., Pautet, P. D., Bossert, K., Criddle, N. R., Reynolds, C. A., Reinecke, P. A., Uddstrom, M., Revell, M. J., Turner, R., Kaifler, B., Wagner, J. S., Mixa, T., Kruse, C. G., Nugent, A. D., Watson, C. D., Gisinger, S., Smith, S. M., Lieberman, R. S., Laughman, B., Moore, J. J., Brown, W. O., Haggerty, J. A., Rockwell, A., Stossmeister, G. J., Williams, S. F., Hernandez, G., Murphy, D. J., Klekociuk, A. R., Reid, I. M., and Ma, J., 2016, The Deep Propagating Gravity Wave Experiment (DEEPWAVE): An Airborne and Ground-Based Exploration of Gravity Wave Propagation and Effects from Their Sources throughout the Lower and Middle Atmosphere: Bulletin of the American Meteorological Society, v. 97, no. 3, p. 425-453.

Gallagher, M. W., Connolly, P. J., Whiteway, J., Figueras-Nieto, D., Flynn, M., Choularton, T. W., Bower, K. N., Cook, C., Busen, R., and Hacker, J., 2005, An overview of the microphysical structure of cirrus clouds observed during EMERALD-1: Quarterly Journal of the Royal Meteorological Society, v. 131, no. 607, p. 1143-1169.

Gasparini, B., and Lohmann, U., 2016, Why cirrus cloud seeding cannot substantially cool the planet: Journal of Geophysical Research-Atmospheres, v. 121, no. 9, p. 4877-4893.

Gayet, J. F., Ovarlez, J., Shcherbakov, V., Strom, J., Schumann, U., Minikin, A., Auriol, F., Petzold, A., and Monier, M., 2004, Cirrus cloud microphysical and optical properties at southern and northern midlatitudes during the INCA experiment: Journal of Geophysical Research-Atmospheres, v. 109, no. D20.

Gettelman, A., Collins, W. D., Fetzer, E. J., Eldering, A., Irion, F. W., Duffy, P. B., and Bala, G., 2006, Climatology of upper-tropospheric relative humidity from the Atmospheric Infrared Sounder and implications for climate: Journal of Climate, v. 19, no. 23, p. 6104-6121.

Gettelman, A., Liu, X., Barahona, D., Lohmann, U., and Chen, C., 2012, Climate impacts of ice nucleation: Journal of Geophysical Research-Atmospheres, v. 117, p. 14.

Gettelman, A., Liu, X., Ghan, S. J., Morrison, H., Park, S., Conley, A. J., Klein, S. A., Boyle, J., Mitchell, D. L., and Li, J. L. F., 2010, Global simulations of ice nucleation and ice supersaturation with an improved cloud scheme in the Community Atmosphere Model: Journal of Geophysical Research-Atmospheres, v. 115, p. 19.

Haag, W., Karcher, B., Strom, J., Minikin, A., Lohmann, U., Ovarlez, J., and Stohl, A., 2003, Freezing thresholds and cirrus cloud formation mechanisms inferred from in situ measurements of relative humidity: Atmospheric Chemistry and Physics, v. 3, p. 1791-1806.

Heymsfield, A. J., and Miloshevich, L. M., 1995, Relative humidity and temperature influences on cirrus formation and evolution: Observations from wave clouds and FIRE II: Journal of the Atmospheric Sciences, v. 52, no. 23, p. 4302-4326.

Hoose, C., and Möhler, O., 2012, Heterogeneous ice nucleation on atmospheric aerosols: a review of results from laboratory experiments: Atmos. Chem. Phys., v. 12, no. 20, p. 9817-9854.

Jensen, E. J., Lawson, P., Baker, B., Pilson, B., Mo, Q., Heymsfield, A. J., Bansemer, A., Bui, T. P., McGill, M., Hlavka, D., Heymsfield, G., Platnick, S., Arnold, G. T., and Tanelli, S., 2009, On the importance of small ice crystals in tropical anvil cirrus: Atmospheric Chemistry and Physics, v. 9, no. 15, p. 5519-5537.

Jensen, E. J., Lawson, R. P., Bergman, J. W., Pfister, L., Bui, T. P., and Schmitt, C. G., 2013, Physical processes controlling ice concentrations in synoptically forced, midlatitude cirrus: Journal of Geophysical Research-Atmospheres, v. 118, no. 11, p. 5348-5360.

Jensen, J., 2017, Personal Email Communication

Kahn, B. H., Gettelman, A., Fetzer, E. J., Eldering, A., and Liang, C. K., 2009, Cloudy and clear-sky relative humidity in the upper troposphere observed by the A-train: Journal of Geophysical Research-Atmospheres, v. 114.

Karcher, B., Hendricks, J., and Lohmann, U., 2006, Physically based parameterization of cirrus cloud formation for use in global atmospheric models: Journal of Geophysical Research-Atmospheres, v. 111, no. D1.

Karcher, B., and Lohmann, U., 2003, A parameterization of cirrus cloud formation: Heterogeneous freezing: Journal of Geophysical Research-Atmospheres, v. 108, no. D14.

Kazil, J., Stier, P., Zhang, K., Quaas, J., Kinne, S., O'Donnell, D., Rast, S., Esch, M., Ferrachat, S., Lohmann, U., and Feichter, J., 2010, Aerosol nucleation and its role for clouds and Earth's radiative forcing in the aerosol-climate model ECHAM5-HAM: Atmospheric Chemistry and Physics, v. 10, no. 22, p. 10733-10752.

Koop, T., Luo, B. P., Tsias, A., and Peter, T., 2000, Water activity as the determinant for homogeneous ice nucleation in aqueous solutions: Nature, v. 406, no. 6796, p. 611-614.

Korolev, A., and Isaac, G. A., 2005, Shattering during sampling by OAPs and HVPS. Part I: Snow particles: Journal of Atmospheric and Oceanic Technology, v. 22, no. 5, p. 528-542.

Korolev, A. V., Emery, E. F., Strapp, J. W., Cober, S. G., Isaac, G. A., Wasey, M., and Marcotte, D., 2011, Small Ice Particles in Tropospheric Clouds: Fact or Artifact? Airborne Icing Instrumentation Evaluation Experiment: Bulletin of the American Meteorological Society, v. 92, no. 8, p. 967-973.

Krämer, M., Schiller, C., Afchine, A., Bauer, R., Gensch, I., Mangold, A., Schlicht, S., Spelten, N., Sitnikov, N., Borrmann, S., de Reus, M., and Spichtinger, P., 2009, Ice supersaturations and cirrus cloud crystal numbers: Atmospheric Chemistry and Physics, v. 9, no. 11, p. 3505-3522.

Kuebbeler, M., Lohmann, U., Hendricks, J., and Kaercher, B., 2014, Dust ice nuclei effects on cirrus clouds: Atmospheric Chemistry and Physics, v. 14, no. 6, p. 3027-3046.

Liu, X., Easter, R. C., Ghan, S. J., Zaveri, R., Rasch, P., Shi, X., Lamarque, J. F., Gettelman, A., Morrison, H., Vitt, F., Conley, A., Park, S., Neale, R., Hannay, C., Ekman, A. M. L., Hess, P., Mahowald, N., Collins, W., Iacono, M. J., Bretherton, C. S., Flanner, M. G., and Mitchell, D., 2012, Toward a minimal representation of aerosols in climate models: description and evaluation in the Community Atmosphere Model CAM5: Geosci. Model Dev., v. 5, no. 3, p. 709-739.

Lohmann, U., Stier, P., Hoose, C., Ferrachat, S., Kloster, S., Roeckner, E., and Zhang, J., 2007, Cloud microphysics and aerosol indirect effects in the global climate model ECHAM5-HAM: Atmospheric Chemistry and Physics, v. 7, no. 13, p. 3425-3446.

McFarquhar, G. M., Um, J., Freer, M., Baumgardner, D., Kok, G. L., and Mace, G., 2007, Importance of small ice crystals to cirrus properties: Observations from the Tropical Warm Pool International Cloud Experiment (TWP-ICE): Geophysical Research Letters, v. 34, no. 13.

Mitchell, D. L., and Finnegan, W., 2009, Modification of cirrus clouds to reduce global warming: Environmental Research Letters, v. 4, no. 4, p. 8.

Mitchell, D. L., Rasch, P., Ivanova, D., McFarquhar, G., and Nousiainen, T., 2008, Impact of small ice crystal assumptions on ice sedimentation rates in cirrus clouds and GCM simulations: Geophysical Research Letters, v. 35, no. 9.

Morrison, H., and Gettelman, A., 2008, A new two-moment bulk stratiform cloud microphysics scheme in the community atmosphere model, version 3 (CAM3). Part I: Description and numerical tests: Journal of Climate, v. 21, no. 15, p. 3642-3659.

Muhlbauer, A., Ackerman, T. P., Lawson, R. P., Xie, S., and Zhang, Y., 2015, Evaluation of cloud-resolving model simulations of midlatitude cirrus with ARM and A-train observations: Journal of Geophysical Research-Atmospheres, v. 120, no. 13, p. 6597-6618.

Murphy, D. M., and Koop, T., 2005, Review of the vapour pressures of ice and supercooled water for atmospheric applications: Quarterly Journal of the Royal Meteorological Society, v. 131, no. 608, p. 1539-1565.

Neale, R. B., Chen, C.-C., Gettelman, A., Lauritzen, P. H., Park, S., Williamson, D. L., Conley, A. J., Garcia, R., Kinnison, D., Lamarque, J. F., Marsh, D., Mills, M., Smith, A. K., Tilmes, S., Vitt, F., Morrison, H., Cameron-Smith, P., Collins, W. D., Iacono, M. J., Easter, R. C., Ghan, S. J., Liu, X., Rasch, P., and Taylor, M. A., 2012, Decription of the NCAR Community Atmopshere Model (CAM 5.0), *in* NCAR, ed., NCAR Technical Note.

O'Donnell, D., Tsigaridis, K., and Feichter, J., 2011, Estimating the direct and indirect effects of secondary organic aerosols using ECHAM5-HAM: Atmospheric Chemistry and Physics, v. 11, no. 16, p. 8635-8659.

Ovarlez, J., Gayet, J. F., Gierens, K., Strom, J., Ovarlez, H., Auriol, F., Busen, R., and Schumann, U., 2002, Water vapour measurements inside cirrus clouds in Northern and Southern hemispheres during INCA: Geophysical Research Letters, v. 29, no. 16.

Park, S., Bretherton, C. S., and Rasch, P. J., 2014, Integrating Cloud Processes in the Community Atmosphere Model, Version 5: Journal of Climate, v. 27, no. 18, p. 6821-6856.

Penner, J. E., Zhou, C., and Liu, X., 2015, Can cirrus cloud seeding be used for geoengineering?: Geophysical Research Letters, v. 42, no. 20, p. 8775-8782.

Petters, M. D., and Kreidenweis, S. M., 2007, A single parameter representation of hygroscopic growth and cloud condensation nucleus activity: Atmospheric Chemistry and Physics, v. 7, no. 8, p. 1961-1971.

Pruppacher, H. R., and Klett, J. D., 1997, Microphysics of clouds and precipitation, Dordrecht ; Boston, Kluwer Academic Publishers, Atmospheric and oceanographic sciences library, v. 18, xx, 954

Shi, X., Liu, X., and Zhang, K., 2015, Effects of pre-existing ice crystals on cirrus clouds and comparison between different ice nucleation parameterizations with the Community Atmosphere Model (CAM5): Atmospheric Chemistry and Physics, v. 15, no. 3, p. 1503-1520.

Soden, B. J., and Held, I. M., 2006, An assessment of climate feedbacks in coupled ocean-atmosphere models: Journal of Climate, v. 19, no. 14, p. 3354-3360.

Stevens, B., Giorgetta, M., Esch, M., Mauritsen, T., Crueger, T., Rast, S., Salzmann, M., Schmidt, H., Bader, J., Block, K., Brokopf, R., Fast, I., Kinne, S., Kornblueh, L., Lohmann, U., Pincus, R., Reichler, T., and Roeckner, E., 2013, Atmospheric component of the MPI-M Earth System Model: ECHAM6: Journal of Advances in Modeling Earth Systems, v. 5, no. 2, p. 146-172.

Storelvmo, T., Boos, W. R., and Herger, N., 2014, Cirrus cloud seeding: a climate engineering mechanism with reduced side effects?: Philosophical Transactions of the Royal Society a-Mathematical Physical and Engineering Sciences, v. 372, no. 2031.

Storelvmo, T., and Herger, N., 2014, Cirrus cloud susceptibility to the injection of ice nuclei in the upper troposphere: Journal of Geophysical Research-Atmospheres, v. 119, no. 5, p. 2375-2389.

Strom, J., Seifert, M., Karcher, B., Ovarlez, J., Minikin, A., Gayet, J. F., Krejci, R., Petzold, A., Auriol, F., Haag, W., Busen, R., Schumann, U., and Hansson, H. C., 2003, Cirrus cloud occurrence as function of ambient relative humidity: a comparison of observations obtained during the INCA experiment: Atmospheric Chemistry and Physics, v. 3, p. 1807-1816.

Stubenrauch, C. J., Chedin, A., Radel, G., Scott, N. A., and Serrar, S., 2006, Cloud properties and their seasonal and diurnal variability from TOVS path-B: Journal of Climate, v. 19, no. 21, p. 5531-5553.

Wofsy, S. C., Team, H. S., Cooperating Modellers, T., and Satellite, T., 2011, HIAPER Pole-to-Pole Observations (HIPPO): fine-grained, global-scale measurements of climatically important atmospheric gases and aerosols: Philosophical Transactions of the Royal Society a-Mathematical Physical and Engineering Sciences, v. 369, no. 1943, p. 2073-2086.

Wu, C., Liu, X., Diao, M., Zhang, K., Gettelman, A., Lu, Z., Penner, J. E., and Lin, Z., 2017, Direct comparisons of ice cloud macro- and microphysical properties simulated by the Community Atmosphere Model version 5 with HIPPO aircraft observations: Atmos. Chem. Phys., v. 17, no. 7, p. 4731-4749.

Zelinka, M. D., Klein, S. A., and Hartmann, D. L., 2012, Computing and Partitioning Cloud Feedbacks Using Cloud Property Histograms. Part I: Cloud Radiative Kernels: Journal of Climate, v. 25, no. 11, p. 3715-3735.

Zelinka, M. D., Klein, S. A., Taylor, K. E., Andrews, T., Webb, M. J., Gregory, J. M., and Forster, P. M., 2013, Contributions of Different Cloud Types to Feedbacks and Rapid Adjustments in CMIP5: Journal of Climate, v. 26, no. 14, p. 5007-5027.

Zhang, K., Liu, X., Wang, M., Comstock, J. M., Mitchell, D. L., Mishra, S., and Mace, G. G., 2013, Evaluating and constraining ice cloud parameterizations in CAM5 using aircraft measurements from the SPARTICUS campaign: Atmospheric Chemistry and Physics, v. 13, no. 9, p. 4963-4982.

Zhang, K., O'Donnell, D., Kazil, J., Stier, P., Kinne, S., Lohmann, U., Ferrachat, S., Croft, B., Quaas, J., Wan, H., Rast, S., and Feichter, J., 2012, The global aerosol-climate model ECHAM-HAM, version 2: sensitivity to improvements in process representations: Atmospheric Chemistry and Physics, v. 12, no. 19, p. 8911-8949.

Zondlo, M. A., Paige, M. E., Massick, S. M., and Silver, J. A., 2010, Vertical cavity laser hygrometer for the National Science Foundation Gulfstream-V aircraft: Journal of Geophysical Research-Atmospheres, v. 115.

8 Appendix

8.1 Formulas

Calculation of RHi

Relative humidity with respect to ice was calculated following:

$$RH_i[\%] = \frac{P^{VXL}}{P^S} \quad (1)$$

where P^{VXL} is the ambient water vapor pressure as given by the VCSEL hygrometer and P^S is the saturation vapor pressure of water with respect to ice, as given by Murphy and Koop (2007):

$$P^S[\text{Pa}] = \exp\left(9.550426 - 5723.265/T + 3.53068 \cdot \ln(T) - 0.00728332T\right) \quad (2)$$

where *T* is the dataset reference air temperature, in Kelvin.

Calculation of Microphysical Parameters

The estimated number concentration (N_i) of IC between 2 μm and 50 μm or greater than 62 μm was calculated from the number concentrations given by the CDP and 2DC:

$$N_i[\text{L}^{-1}] = N_{2DC} + N_{CDP} \quad (3)$$

where N_{2DC} is the number concentration, in L^{-1}, detected by the 2DC and N_{CDP} is the number concentration detected by the CDP probe, in L^{-1}.

The average diameter of IC between 2 μm and 50 μm or greater than 62 μm was calculated from the average diameters of the IC populations detected by the CDP and 2DC:

$$D_{mean}[\mu\text{m}] = \frac{N_{2DC} \cdot (D_{2DC}) + N_{CDP} \cdot (D_{CDP})}{N_{2DC} + N_{CDP}} \quad (4)$$

where D_{2DC} is the average diameter of IC detected by the 2DC, in μm, and D_{CDP} is the average diameter of IC detected by the CDP, in μm.

8.2 Seasonal Variation in Model Output

Seasonal variation for different CAM5 output parameters is shown below. Each line represents the average of a single season (e.g., MAM in Year 3). The most significant variation in terms of order of magnitude occurs in accumulation aerosol concentration, which varies by a factor of about 2 between the southern autumn (MAM) and spring (SON).

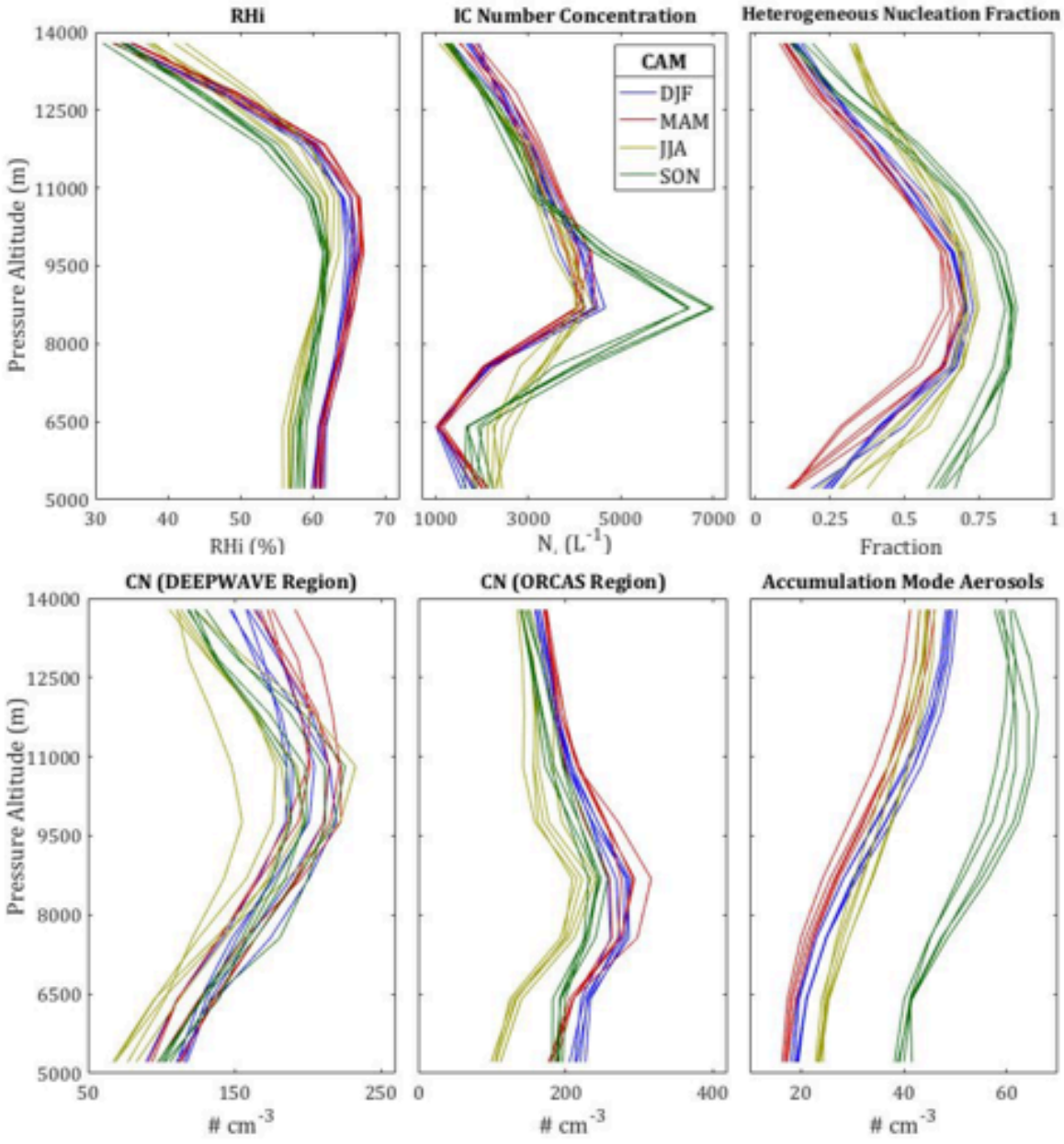

Seasonal variation for ECHAM-HAM is shown below. Again, each line represents the average of a single season in a single year. The most significant variation in terms of order of magnitude occurs for aerosol concentrations. Both CN and accumulation mode aerosols vary by a factor of about three throughout the year, though the peak accumulation mode aerosol concentration does not correspond in time to the peak CN concentration.